

LEN-3211  
IN-20  
126219  
P14

NASA CR-190761



ADVANCED ELECTRIC PROPULSION RESEARCH - 1991

Prepared for  
LEWIS RESEARCH CENTER  
NATIONAL AERONAUTICS AND SPACE ADMINISTRATION

Grant NGR-06-002-112

Annual Report

Jeffery M. Monheiser

October 1992

Approved by

Paul J. Wilbur  
Department of Mechanical Engineering  
Colorado State University  
Fort Collins Colorado 80523

N93-11608

Unclas

G3/20 0126219

(NASA-CR-190761) ADVANCED ELECTRIC  
PROPULSION RESEARCH, 1991 Annual  
Report, 1 Jan. - 31 Dec. 1991  
(Colorado State Univ.) 74 p

*Handwritten signature*

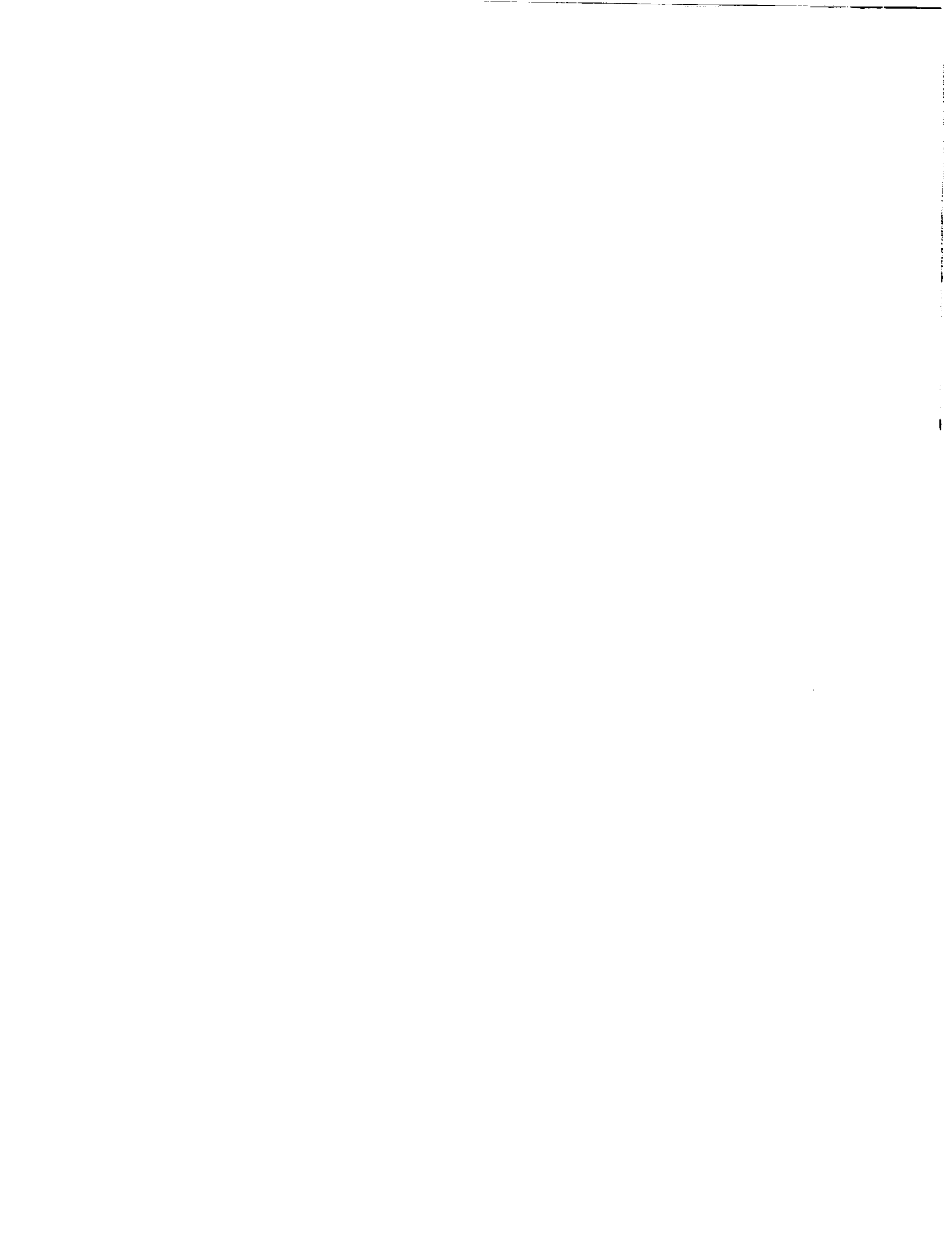


## Table of Contents

Table of Contents . . . . .	ii
List of Figures . . . . .	iii
List of Tables . . . . .	v
Introduction . . . . .	1
First-Order Impingement-Ion-Production Theory . . . . .	2
Discrepancies between Model Predictions and Measurements . . . . .	8
Experimental Apparatus and Procedures . . . . .	11
Erosion Pattern and Rate Tests . . . . .	14
Neutral Velocity Experiment . . . . .	15
Impingement Current and Potential Measurement Tests . . . . .	17
Results . . . . .	25
Comparative Erosion Data for Molybdenum and Graphite Accel Grids . . . . .	25
Effect of Gas Backfill on Impingement Current . . . . .	32
High-Energy Neutral Backflow Experiment . . . . .	34
Potential Fluctuation Experiments . . . . .	38
Effects of Thruster Operating Conditions on Beamlet Potentials and Impingement Currents . . . . .	40
Comparative Floating Potential and Current Density Measurements . . . . .	54
Conclusions . . . . .	58
References . . . . .	60
Distribution List . . . . .	62



## List of Figures

<u>Figure</u>	<u>Title</u>	<u>Page</u>
1	Conceptual, Beamlet-Centerline Potential Profile for Two-Grid Ion Optics	3
2	Emissive-Probe-Floating-Potential Map Downstream of SHAG 15-cm Dia. Grids (potentials in V)	9
3	Electrical Schematic	13
4	High-Energy Reflected-Neutral-Atom Test Apparatus	16
5	Seven-Hole Grid System Configuration	18
6	Beamlet Diagnostic Probes	19
7	3-D Probe Positioning Apparatus	20
8	Emissive Probe Characteristic Curve Measured in 7-hole Grid Set	23
9	Photograph of Molybdenum Grid - 50 hr Erosion Test	27
10	Erosion Depth Profiles at Outer Apertures - 50 hr Test	29
11	Erosion Depth Profiles near Central Aperture - 50 hr Test (Absolute Height Comparisons between Profiles are not Meaningful)	30
12	Effects of Backfill on Impingement Current	33
13	Effects of Target Insertion on Impingement Behavior	36
14	Effect of Discharge Power Supply on Floating Potential Maps (15 cm dia. SHAG Optics Beam)	39
15	Power-Spectral-Density Map Comparison	41
16	Computed and Measured Potential Profiles - No Plasma Case	43
17	Centerline Potential Profile with Beam Extraction	46



<u>Figure</u>	<u>Title</u>	<u>Page</u>
18	Typical Beamlet and Trough Potential Profiles	48
19	Beamlet and Trough Potential Profiles - Neutralizer off	50
20	Effect of Neutralizer Bias on Charge-Exchange Ion Extraction Length	52
21	Effects of Perveance on Charge-Exchange Ion Extraction Length and Impingement-to-Beam Current Ratio	53
22	Effect of Background Xenon Density on Charge-Exchange Length and Impingement Current	55
23	Comparison of Floating-Potential and Beamlet-Current-Density Maps as a Function of Axial Position	56



## List of Tables

<u>Table</u>	<u>Title</u>	<u>Page</u>
1	50 Hour Erosion Test Operating Conditions And Results	26



## Introduction

Ions that impinge on the accelerator (accel) grid of an ion thruster will cause sputter erosion of this grid, thereby limiting its useful lifetime. These ions fall into two general categories, namely, those that originate in the discharge chamber and impinge directly on the accel grid (errant beamlet ions) and those produced near the accel grid that have insufficient energy to escape the potential well that surrounds this grid (low-energy ions). Ions in the first general category are of less concern because errant-beamlet-ion impingement can be reduced to a negligible level by proper design and operation of the grid system. Low-energy ions, on the other hand, are created via the interaction of particles present in the vicinity of the accel grid of a properly designed and operating grid system. While steps can be taken to minimize the current of these ions, complete elimination is not likely with current technology.

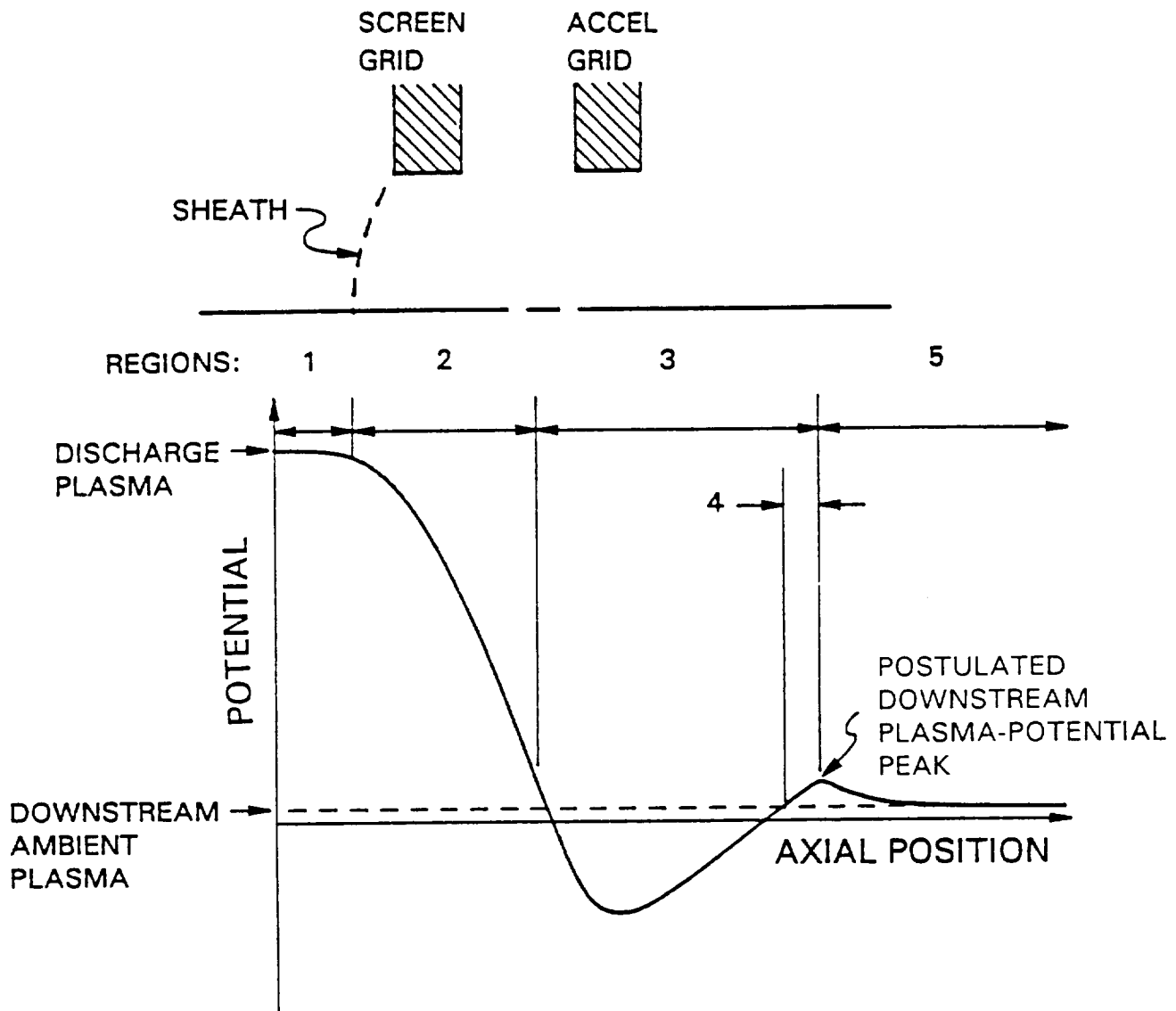
Impingement erosion of accel grids by low-energy ions, while always present, is worse for the operating conditions imposed by some missions. For example, the Derated Ion Thruster [1] achieves a reasonable thrust density at low specific impulse by operating at a low net-to-total accelerating voltage ratio. Under this condition, the sputter yield associated with the ions incident on the accel grid can increase to the point where the grid becomes the life-limiting component of the thruster. It is important to understand low-energy-ion production and collection phenomena so accel-grid lifetimes can be computed and the effects of operating-condition changes like those being investigated for the Derated Ion Thruster can be predicted.

An early study of accel-grid-impingement-ion erosion by Kerslake [2] yielded

a simple one-dimensional model which can be used to estimate low-energy-ion currents to accel grids for two-grid ion extraction systems. While the model yielded reasonable results for mercury thrusters operated in facilities at low pressures, there is evidence that it may not describe experimental results obtained with inert-gas propellants which are typically tested at higher facility pressures [3]. In order to address deficiencies associated with this model, Peng, et al. [4] have developed a numerical procedure which can be applied to predict the production distribution of low-energy ions and their subsequent trajectories into the accel grid in three dimensions. One objective of this paper is to expand the Kerslake model to include additional (e.g. test facility) effects and to then apply it to compute impingement currents that can be compared with experimental results obtained in an inert-gas test environment. A second objective is to compare the sputter-erosion behavior of graphite and molybdenum grids in this same environment. Realization of these objectives should also lead to increased understanding of low-energy-ion-production and accel-grid-impingement processes.

### **First-Order Impingement-Ion-Production Theory**

A qualitative profile of the electrical potential along the centerline of the screen and accel grid apertures in a typical two-grid set is shown in Fig. 1. The volume circumscribed by the apertures and extending over the axial range indicated on the figure will contain ions, electrons and neutral atoms, each at density levels that vary with position. For example, the density of thrust-producing beamlet ions, present throughout the volume, will decrease as they are accelerated from the sheath in accordance with the



- REGION 1: DISCHARGE PLASMA
- REGION 2: BEAMLET ION ACCELERATION
- REGION 3: CHARGE-EXCHANGE IMPINGEMENT ION PRODUCTION
- REGION 4: ELECTRON-IMPACT IMPINGEMENT ION PRODUCTION
- REGION 5: DOWNSTREAM AMBIENT PLASMA

Fig. 1      Conceptual, Beamlet-Centerline Potential Profile for Two-Grid Ion Optics

laws of space-charge-limited particle flow [5]. Neutral propellant atoms will also be present throughout the volume, and their density distribution will be defined by free-molecular flow mechanics [6] reflecting the effects of direct flow from the discharge chamber and back flow from the ambient downstream environment. Electrons, which will generally have low energies, on the other hand, will be present only in the discharge plasma (Region 1 in Fig. 1) and in Regions 4 and 5 (i.e. throughout the downstream plasma and upstream past the potential peak to the point where the potential decreases to the value in the downstream ambient plasma). Particle interactions that result in significant low-energy ion production in these regions occur between beamlet ions and atoms (charge exchange), and electrons and atoms (electron impact). Charge exchange, which involves electron transfer from a slow-moving neutral atom to a fast-moving beamlet ion, results in a fast-moving atom that escapes from the grid region and a low-energy ion which may impinge on the accel grid. Electron impact involves ionization of neutral atoms by electrons that are accelerated from the downstream ambient plasma through the postulated downstream potential peak shown in Fig. 1.

Charge-exchange ions can be produced throughout the regions shown in Fig. 1, but those created within Region 3 are most likely to impinge on the accel grid. This is the case because ions produced there have insufficient kinetic energy to escape the potential well surrounding the accel grid. They will actually reach it on complex trajectories determined by axial fields like those suggested in Fig. 1 and radial fields that are not indicated. In contrast to charge-exchange ions produced in Region 3, those produced in Regions 1 and 2 will acquire sufficient kinetic energy to carry them over the

downstream potential peak away from the accel grid. Finally, charge-exchange ions produced in Region 5 will find themselves in a potential field that draws them downstream away from the accel grid.

Electron-impact ions are also created with a small kinetic energy, so like charge-exchange ions, their trajectories are determined by electric fields in the region where they are created. Electrons capable of producing these ions are accelerated from the downstream ambient plasma (Region 5) through the downstream potential peak and then decelerated until they are reflected at the upstream end of Region 4. Depending on the height of the potential peak, electrons may acquire sufficient kinetic energy to induce ionization in both Regions 4 and 5, however, only the ions produced in Region 4 will find themselves in an electric field that will draw them upstream toward the accel grid.

Charge-exchange ions produced in Region 3 and electron-impact ions produced in Region 4 are trapped in a potential well from which escape generally involves accel grid impingement. The impingement current can be computed, assuming errant-beamlet-ion impingement is negligible, by summing the productions rates of the two groups of low-energy ions. The differential rate of production of low-energy ions due to these processes  $d\dot{n}_V$  in a differential volume  $dV$  where the neutral atom density is  $n_0$ ; the beamlet ion density and velocity are  $n_i$  and  $v_i$ , respectively; the ionizing electron density and velocity are  $n_e$  and  $v_e$ , respectively, and the charge-exchange and ionization cross-sections are  $\sigma_{ce}$  and  $\sigma_e$ , respectively, is given by

$$d\dot{n}_V = n_i n_0 \sigma_{ce} v_i dV + n_e n_0 \sigma_e v_e dV \quad . \quad (1)$$

The beamlet ion current ( $\dot{J}_B$ ) is given by

$$\dot{J}_B = e n_i v_i A_B \quad , \quad (2)$$

where  $e$  is the charge on beamlet ions. Assuming uniform ion and electron densities and velocities over cross-sectional areas associated with both the beamlet ions ( $A_B$ ) and the ionizing electrons ( $A_e$ ) at each axial location ( $z$ ), a one-dimensional form of Eq. 1 can be obtained using Eq. 2 and it can be then simplified into the following form

$$d\dot{n}_v = \frac{1}{e} \dot{J}_B n_o \sigma_{ce} dz + n_e n_o \sigma_e v_e A_e dz \quad . \quad (3)$$

The impingement current associated with each beamlet is obtained from Eq. 3 by multiplying the low-energy ion charge ( $e$ ) and integrating over the axial lengths from which charge-exchange- and electron-impact-produced ions can be drawn to the accel grid. From the discussion of Fig. 1 it is apparent these lengths are those associated with Region 3 (the charge-exchange ion extraction length -  $\ell_{ce}$ ) and Region 4 (the electron-impact ion extraction length -  $\ell_{ei}$ ), respectively. Performing these integrations, the following expression for the impingement current due to each individual beamlet is obtained

$$J_{i,v} = \int_{\ell_{ce}} \dot{J}_B n_o \sigma_{ce} dz + e \int_{\ell_{ei}} n_e n_o \sigma_e v_e A_e dz \quad . \quad (4)$$

Because the beamlet current ( $\dot{J}_B$ ) is independent of axial position and the charge-

exchange-collision cross-section is only mildly dependent on position (ion energy variations expected in this region of a beamlet do not affect it significantly), both can be removed from under the integral sign to obtain

$$J_{i,v} = J_B \sigma_{ce} \int_{\ell_{ce}} n_o dz + e \int_{\ell_{ei}} n_e n_o \sigma_e v_e A_e dz \quad . \quad (5)$$

Equation 5 pertains to individual beamlets, but it can be applied to the many beamlets that make up an ion beam by summing their individual contributions. If neutral-atom density is assumed uniform over the entire grid cross section, Eq. 5 shows the total impingement current due to charge-exchange (the 1<sup>st</sup> term) is directly proportional to total beam current ( $J_B$ ), a quantity which is measured readily. For this study, two limiting axial profiles of neutral density are used. The upper limit is based on the assumption of uniform, axial atomic flow (no divergence) and the lower limit is computed numerically using a model based on atom emission with a cosine distribution from the surface of a multi-hole accel grid [3]. The charge-exchange cross-section can be estimated from the applied screen voltage, hence, the major unknown associated with the first term of Eq. 5 is the charge-exchange ion extraction length -  $\ell_{ce}$ . An objective of this research will, therefore, be to establish a procedure for determining this length experimentally.

The second integral in Eq. 5 is more difficult to evaluate because the quantities appearing under the integral sign are strong functions of axial position. It is appropriate, therefore, to determine if this integral can be neglected compared to the first

one before expending effort to simplify and evaluate it.

### **Discrepancies between Model Predictions and Measurements**

During the preceding grant period floating-emissive-probe measurements had been made [3] in the 15 cm dia. ion beam downstream of accel grid of the modified Space Electric Rocket Test II (SERT II) thruster [7]. This thruster employed conventional small hole accelerator grids (SHAG) and the measurements yielded typical emissive-probe-floating-potential profiles similar to those shown in Fig. 2. Positions on the plot are measured relative to the downstream surface of the accel at the thruster centerline and floating potentials are measured relative to ground. In evaluating these data, it was assumed low-energy ions were produced solely by charge exchange and it was determined they would be drawn back into the accel grid from the shaded region shown in the figure. Hence, the length of this region was considered a reasonable estimate of the charge-exchange ion extraction length. Using this length, the first term in Eq. 5 was applied to determine a volume-integrated impingement current,  $J_{iV} = 0.13$  mA, assuming no production due to electron-impact ionization. The directly-measured impingement current,  $J_{id} = 2.1$  mA, was, however, an order of magnitude larger than the volume-integrated value as indicated on Fig. 2. This level of discrepancy was typical of results obtained in that study [3]. The following possible reasons for this large discrepancy are postulated:

1. The directly-measured impingement current could be in error because of

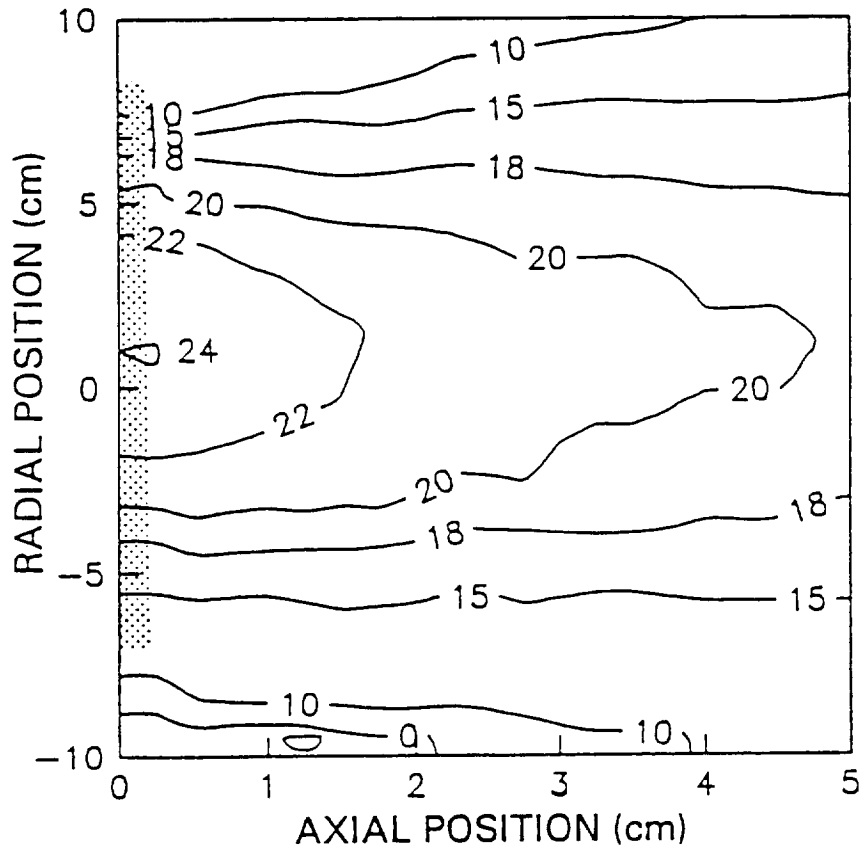


Fig. 2 Emissive-Probe-Floating-Potential Map Downstream of SHAG 15-cm Dia. Grids (potentials in V)

secondary electron emission induced as a result of ion impingement on the accel grid, or

2. The volume-integrated impingement current could be in error because:
  - a) electron-impact ionization, which had been postulated as small, is actually much greater than the charge-exchange component,
  - b) published charge-exchange cross-section data are in error,
  - c) calculated, axial neutral-density profiles are incorrect, or
  - d) measured charge-exchange ion extraction lengths are in error because:
    - i) propellant or background atoms have energies greater than what have been expected to be negligible thermal values,
    - ii) fluctuations in the potentials downstream of the ion source cause the ion extraction lengths to fluctuate with time or
    - iii) measurements of the potentials downstream of the ion source used to establish ion-extraction lengths are inaccurate.

In order to determine which of these factors might be causing the order-of-magnitude difference between directly-measured and volume-integrated impingement currents, each was evaluated.

Examination of published data on secondary-electron emission coefficients [8] suggests that an error of 2% in the directly-measured impingement current is the most that could develop as a result of secondary-electron emission from the accel grid. This error is far less than the order of magnitude error experienced so it is concluded that secondary-electron emission from the accel grid should be negligible. A similar search

of the literature showed that published charge-exchange cross-section data differ only slightly between authors [9], and this suggested an error in the cross-section data is unlikely.

To determine if the analysis used to compute neutral density profiles were in error, an extreme case was considered. It was assumed that the neutral density remained invariant with axial position at the value computed within the discharge chamber by applying the free-molecular flow, sharp-edged orifice equation at the specified discharge-chamber propellant flow rate [6]. Introducing the geometrical data for the SHAG grid set being used yielded a neutral density that induced a 80% increase in the volume-integrated impingement current; however, the volume-integrated impingement current obtained using this extreme neutral density profile was still  $\sim 1/5$  of the measured impingement current. These results suggest that the discrepancies between the measured and volume-integrated impingement current must be due to either a substantial electron-impact ionization contribution or inaccuracies associated with the measurement of the charge-exchange-ion extraction length. Hence it was concluded that experiments should be performed to evaluate these two possibilities.

### **Experimental Apparatus and Procedures**

Experiments conducted during this grant period were also carried out using the SERT II thruster modified to incorporate a movable, inert-gas-hollow-cathode neutralizer and independent main and hollow-cathode flow systems that facilitate

discharge chamber operation on inert-gas propellants [7]. Figure 3 shows electrical connections between various power supplies and the thruster and neutralizer as well as the symbols that represent the various currents and voltages measured. Some of these experiments used SHAG grids that produced a 15-cm-dia. beam. For other tests, however, the discharge chamber was masked down to accommodate grids that produced beam diameters of 3.2 or 1.2 cm. Because these masked-down grid sets were positioned on the thruster centerline where discharge plasma properties are uniform to within a few percent, all of these apertures should have been exposed to the same plasma density.

Masked-down grid tests involved the use of three different grid sets of two designs. One design, used to determine grid erosion patterns and rates, included a set made from poly-crystalline synthetic graphite (Poco Graphite Inc., AXF-5Q) with a density of  $1.8 \text{ g/cm}^3$  and a set made from molybdenum with a density of  $10.2 \text{ g/cm}^3$ . The second design was used when potential measurements were being made to determine the lengths of the various regions indicated in Fig. 1. Grids of a given design were operated at a standard condition. For example, the erosion grid tests were conducted at screen ( $V_+$ ) and accel ( $V_-$ ) voltages of 1000 V and -800 V, respectively, a beam current ( $J_B$ ) of 4.3 mA, and impingement current ( $J_{id}$ ) of  $100 \mu\text{A}$  and a total thruster flow rate ( $\dot{m}_T = 39 \text{ mA eq.}$ ) which induced an ambient vacuum-tank pressure of  $7 \times 10^{-6}$  Torr. The potential measurement tests were conducted at screen ( $V_+$ ) and accel ( $V_-$ ) voltages of 1000 V and -500 V, respectively, beam currents ranging from 0.25 to 1.5 mA, impingement currents ranging from 25 to  $80 \mu\text{A}$  and a total thruster flow rate ( $\dot{m}_T$ ) of 46 mA eq. which also induced an ambient vacuum-tank pressure near  $7 \times 10^{-6}$  Torr.

THRUSTER

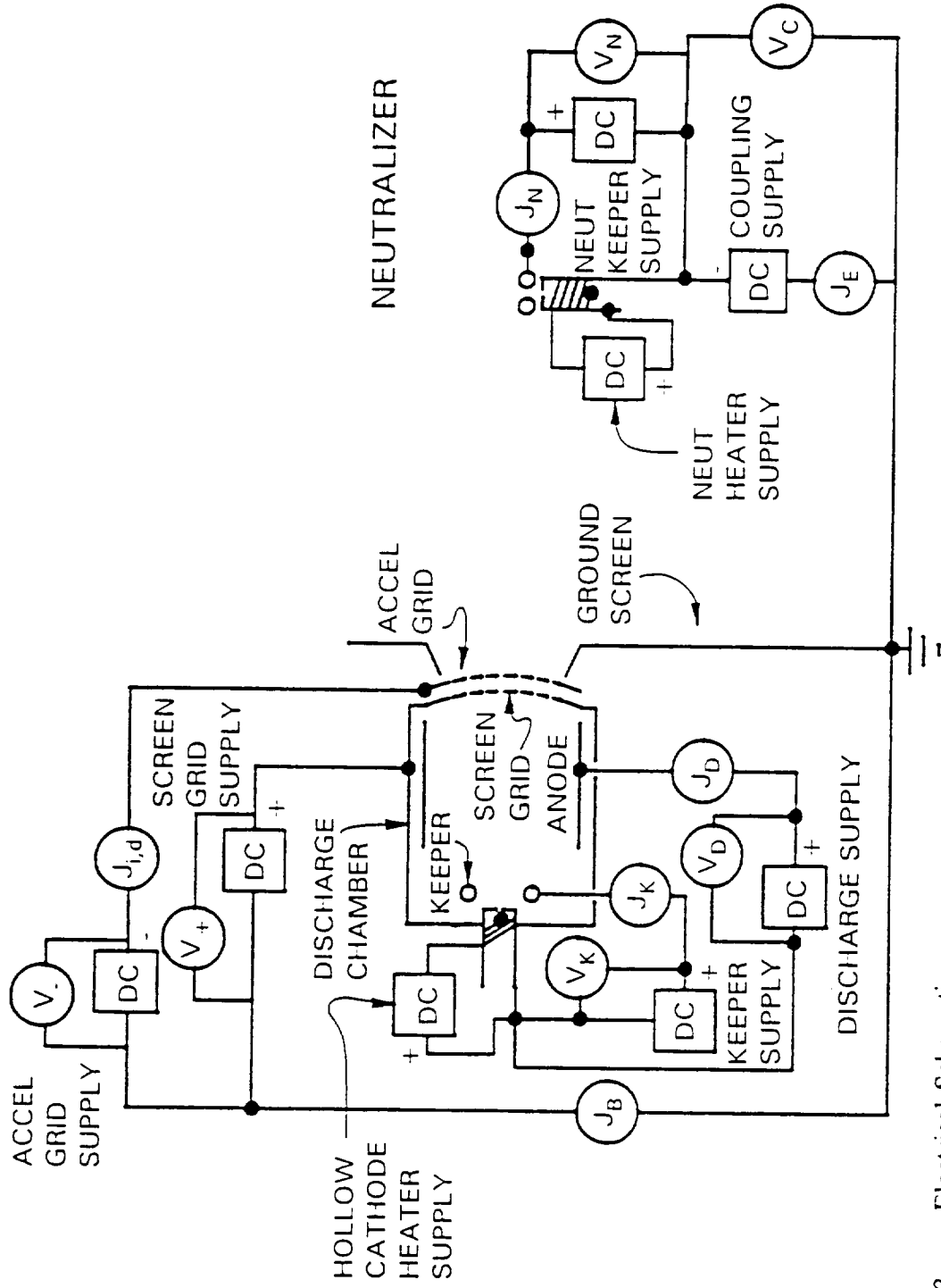


Fig. 3 Electrical Schematic

Special meters suitable for measuring the small beam and impingement currents to an accuracy of  $\pm 5\%$  were installed. The impingement current meter was installed on the negative high voltage side of the accel grid supply because small leakage currents associated with the supply induced significant errors when it was installed on the ground side. Unless noted otherwise, beam neutralization was accomplished using a xenon hollow-cathode neutralizer that was biased sufficiently negative so it would emit an electron current that would meet or exceed the ion beam current. It was positioned near the beam centerline 20 cm downstream of the accel grid. All tests were conducted in a diffusion-pumped, 1.2 m dia. by 5.4 m long, stainless steel vacuum chamber using xenon as the propellant. The charge-exchange cross-section for this propellant at the screen voltage used for all tests (1000 V) is  $38 \times 10^{-16} \text{ cm}^2$  [9].

#### Erosion Pattern and Rate Tests

Comparative erosion tests were conducted by operating 19-hole molybdenum and then graphite grid sets at the standard operating condition, which had been selected so direct ion impingement would be negligible. Minimum direct impingement was demonstrated by showing the impingement-to-beam-current ratio remained constant as  $V_+$  and  $V_-$  were varied on either side of their operating values. Grid sets with a hole pattern that was geometrically similar to that of typical high-perveance sets, had 2.0 mm screen and accel hole diameters on 2.5 mm center-to-center separations (58% open area fraction), 0.51 mm grid thicknesses and a 0.51 mm grid-to-grid separation distance. For

both the graphite and molybdenum accel grids, the masses and flatness profiles over radial and circumferential spans of  $\sim 2.5$  mm were measured using, respectively, a balance accurate to  $\pm 10 \mu\text{g}$  and a profilometer accurate to  $\pm 0.01 \mu\text{m}$ . After installation on the thruster, each grid set was operated for 50 hr. at the aforementioned standard condition and then disassembled so mass and profilometric measurements could be repeated. The appearance of the grids was also recorded photographically at various magnifications and the microscope objective translation required to achieve focus at different locations was used to verify profilometric results.

#### Neutral Velocity Experiment

In order to determine if significant numbers of neutral atoms could be ionized downstream of the downstream potential peak (Fig. 1) and still be able to overcome the adverse potential gradient created by the peak and reach the accel grid, a simple experiment was conducted using the 15 cm dia. SHAG grid set and the test configuration shown in Fig. 4. The test involved operation of the thruster with its xenon ion beam directed toward the 30 cm x 30 cm planar Grafoil<sup>1</sup> and copper target assembly shown. These targets could be rotated so they intercepted the entire beam in the manner suggested in the figure, or they could also be rotated  $90^\circ$  to the ion beam thereby allowing it pass between the two targets and impinge on a stainless steel target 520 cm downstream of the thruster. It is argued that high-energy xenon neutrals that could be

---

<sup>1</sup> Grafoil is a flexible graphite manufactured by Union Carbide Corp.

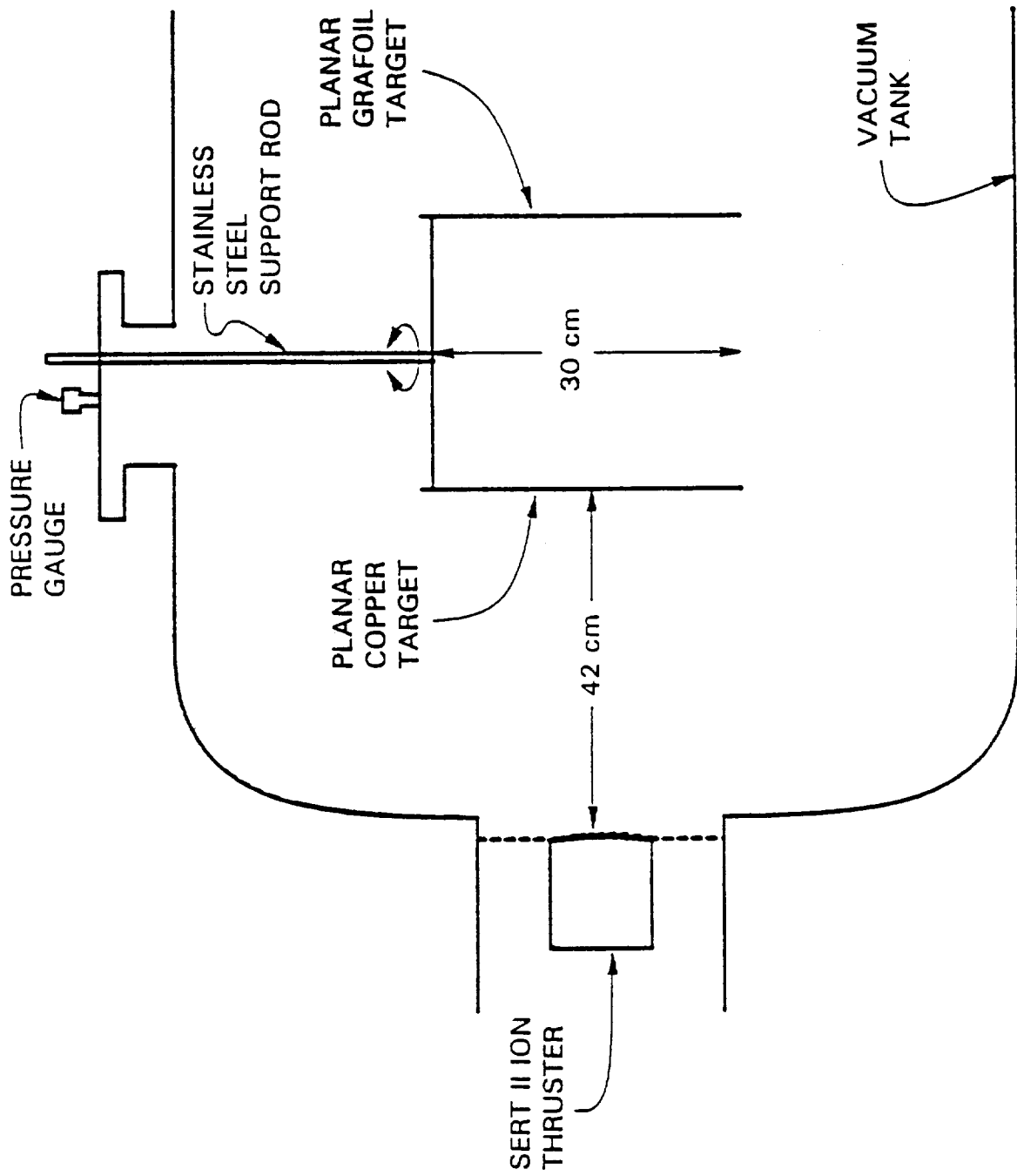


Fig. 4 High-Energy Reflected-Neutral-Atom Test Apparatus

created and reflected back when beam ions recombine at these surfaces would exhibit very different production rates and energies for the three situations (two nearby target surfaces of different materials and a distant surface).

### Impingement Current and Potential Measurement Tests

Preliminary tests conducted with SHAG grid sets showed that the spatial resolution of available probing techniques was inadequate to yield accurate potential-profile data of the sort shown qualitatively in Fig. 1 [3]. Consequently, a graphite grid set with seven large holes and the dimensions and configuration shown in Fig. 5 was installed on the thruster. This 7-hole grid set, which produces an ion beam diameter of 3.2 cm, is designed to facilitate potential measurements across the accel grid surface and upstream through the accel and screen grid holes. Because of the large grid aperture diameter and grid spacings, beam currents that could be extracted at the applied voltages were small. Neutral densities, on the other hand, had to be sufficient to sustain the plasma discharge. As a result, the thruster operated at low propellant utilization efficiencies. Because beam current and neutral loss effects can be separated (Eq. 5), however, this did not affect the usefulness of the experimental results.

Electrical potentials were measured using the hot-filament emissive probe shown on Fig. 6a. The loop of 0.05 mm dia. tungsten wire ( $\sim 3$  mm x 3 mm) is considered sufficiently small compared to the dimensions of the grids shown in Fig. 5 to yield potential data with acceptable spatial resolution. The probe is supported from an

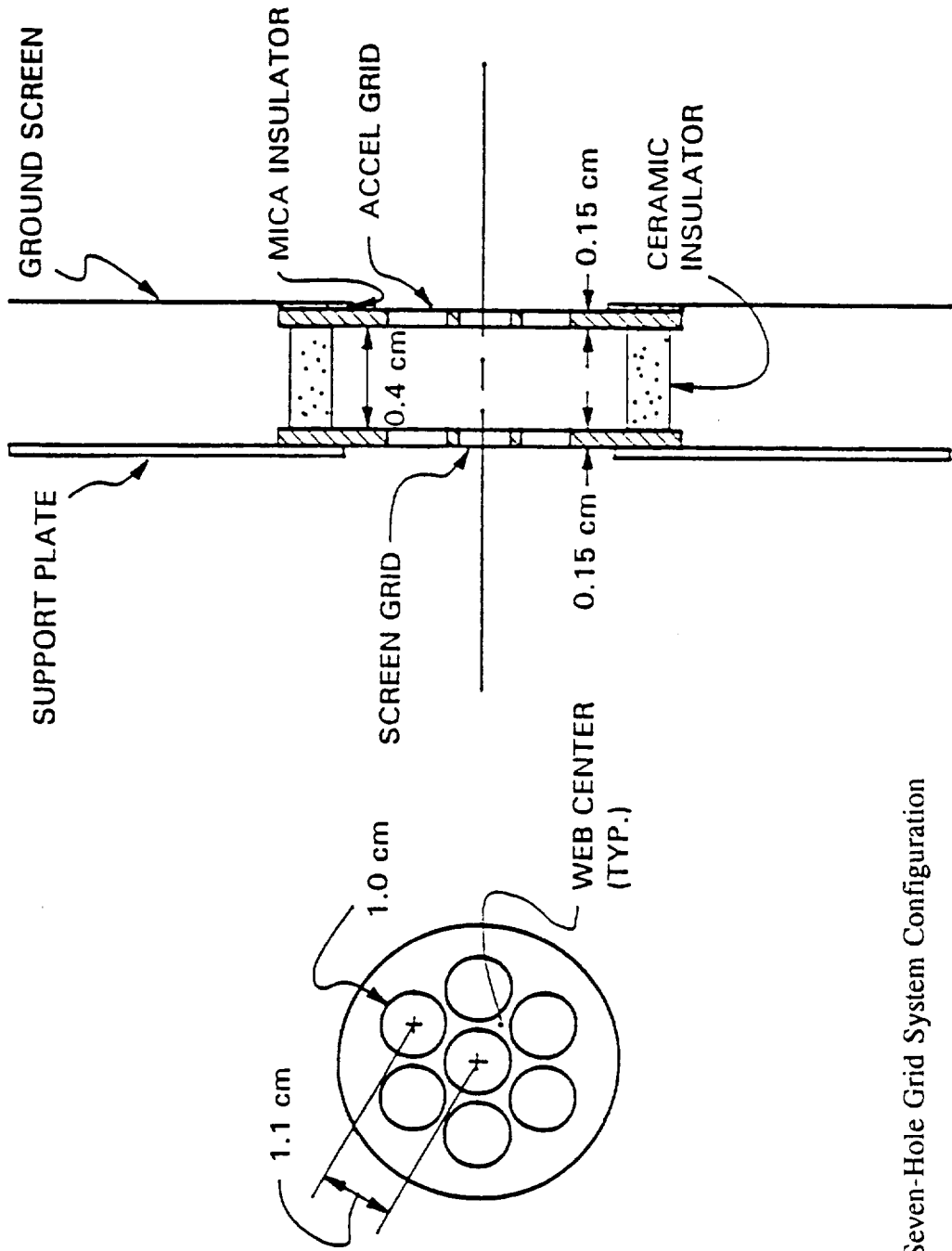
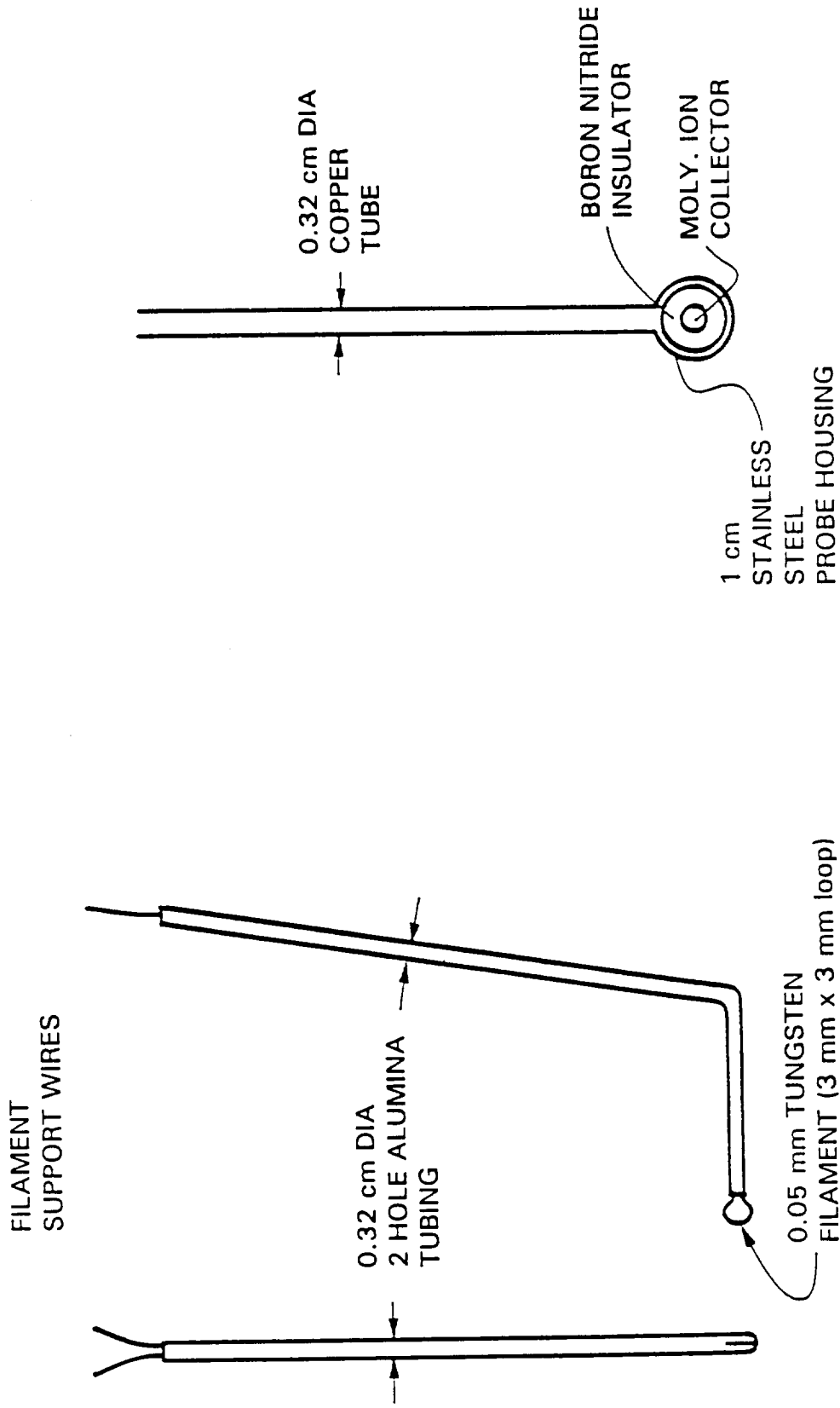


Fig. 5 Seven-Hole Grid System Configuration



a) Emissive Probe

b) Planar Current-Density Probe

Fig. 6 Beamlet Diagnostic Probes

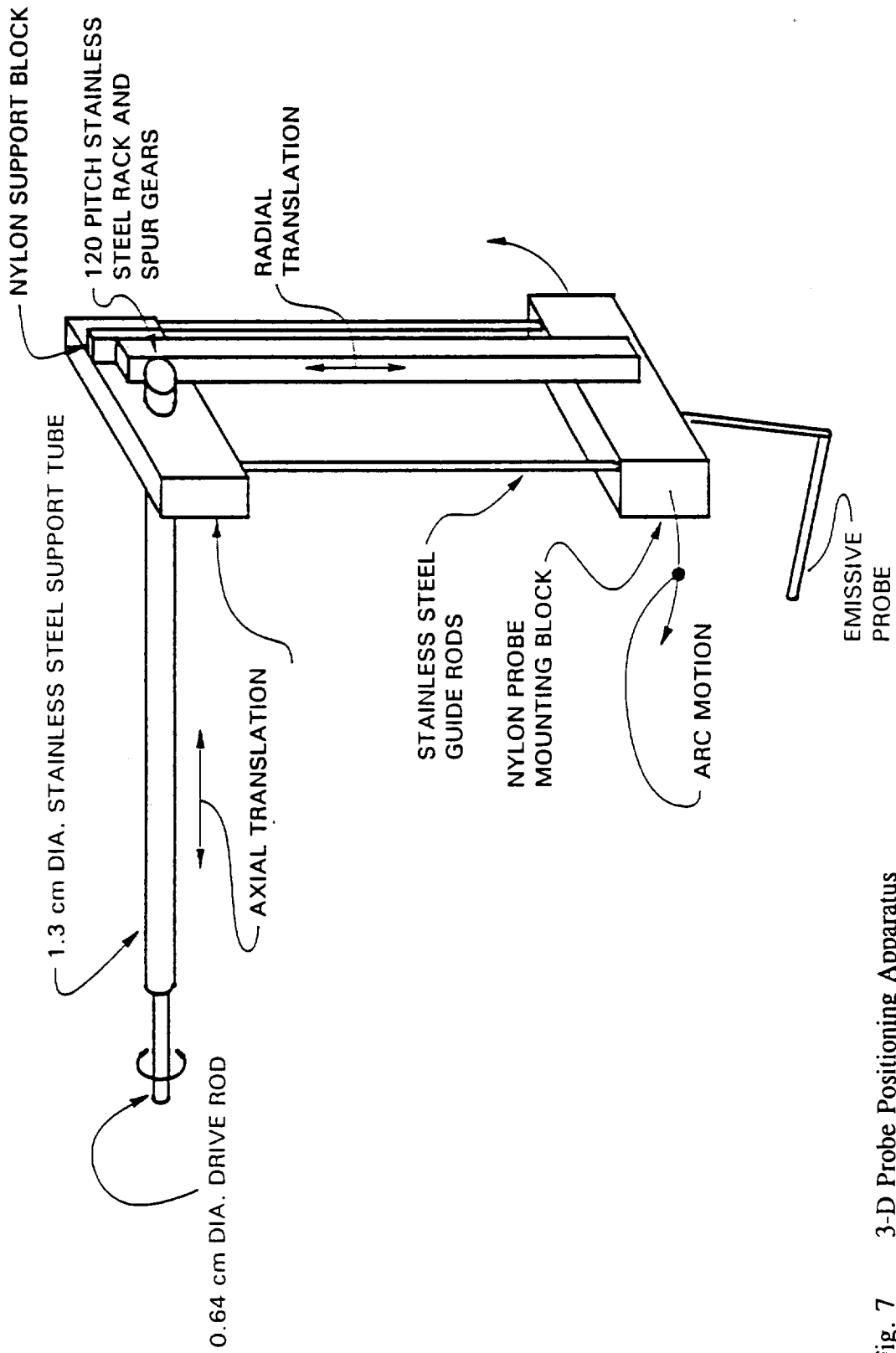


Fig. 7 3-D Probe Positioning Apparatus

alumina rod attached to a positioning assembly (Fig. 7) that can be used to translate the loop either along the beamlet centerline through the center hole or along a parallel trajectory that intersects the accel grid at the web center (Fig. 5). The axial position of the loop, which was measured from the downstream edge of accel grid to the upstream tip of the loop, is adjusted via a micrometer. The assembly shown in Fig. 7 can also be used to sweep the probe along arcs of various radii centered at the 1.3 cm dia. stainless steel support tube. In this operating mode, potential measurements can be made over a planar surface perpendicular to the beamlets at a prescribed downstream axial position. The collector of the current-density probe shown in Fig. 6b was biased sufficiently negative of ground ( $\sim 30$  V) so electrons would be reflected from it and the collector surface would sense only the current due to low-energy and beam ions. This probe was also attached to the positioning assembly so it could be swept along arcs of various radii from the support tube through the beamlets to measure ion-beam-current-density profiles. Radial and axial positions of either the emissive probe loop or the current density sensor are considered accurate to within  $\pm 0.3$  mm.

The emissive probe shown in Fig. 6a was operated by passing sufficient direct current through the loop ( $\sim 1$  A) to heat it resistively to thermionic emission (incandescent) temperatures. In many plasmas, such a loop (or filament) will float near local plasma potential and this floating potential can be sensed directly [10]. The conditions required for this method to yield accurate results are, however, not satisfied in the electron-deficient environment close to the accel grid. Generally, accurate potentials can be obtained in such an environment if the electron emission current from

the loop is measured as a function of the potential applied to it and the resulting curve is analyzed to identify the "inflection-point" potential at which electron emission begins [11]. Local potential measurements in the vicinity of the accel grid are complicated not only because electron densities are depleted, but also because the measurements are made in a beam of high-energy ions. Still, it appears that reasonably accurate potentials can be obtained in this region by interpreting plots of filament emission current as a function of the potential applied to it.

Figure 8 shows a typical example of a probe emission current v. potential curve measured on a beamlet centerline 14 mm downstream of the accel grid using ground as the reference potential in a test where the neutralizer was off. Traces produced with the neutralizer exhibit the same general behavior as the one shown in Fig. 8 although the potentials are shifted generally to more negative values. As the dotted lines on the figure suggest, the potential at the probe location (local potential) is determined by finding the intersection between two adjacent, relatively straight-line segments of the curve. One line is tangent to the segment where the filament emission current breaks upward and the other is through the nearly-horizontal, linear portion where electrons would be collected if they were present. This procedure is justified by the following physical arguments pertaining to a probe surface in a beamlet environment. When the probe filament is positive of local potential, Fig. 8 shows it still exhibits a positive electron emission current. This condition exists because the probe is being hit by beamlet ions and they affect probe current in the same way emitted electrons do. As the probe is biased more positive, the current can decay because 1) some beamlet ions

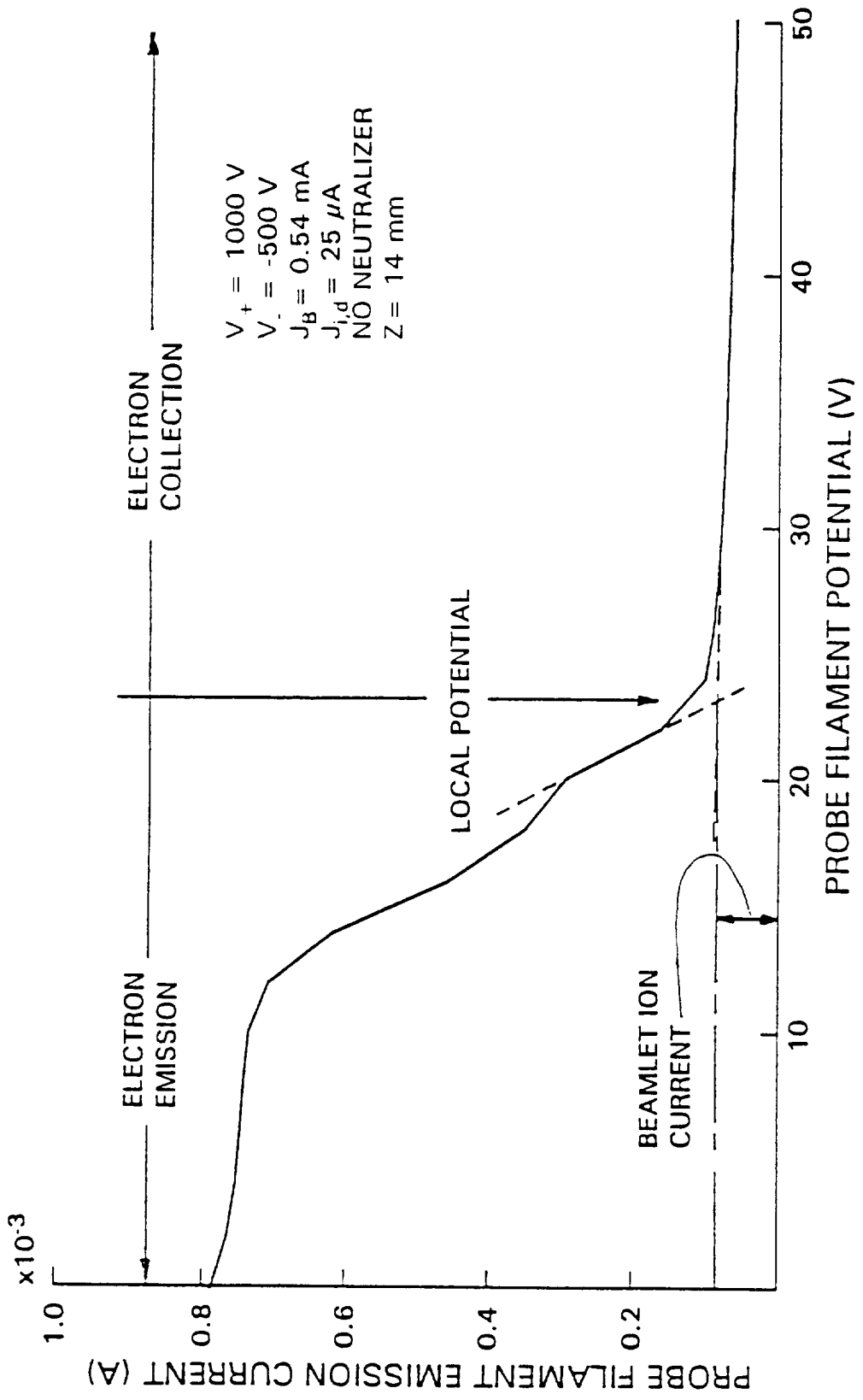


Fig. 8 Emissive Probe Characteristic Curve Measured in 7-hole Grid Set

begin to be deflected away from it and 2) electrons, which may be present at the probe location, begin to be collected. On the other hand biasing the probe below local potential facilitates electron emission from the incandescent filament surface. As Fig. 8 shows, the electron-emission portion of the curve contains a great deal of structure that is presumably influenced in large measure by space-charge effects. Axial potential profiles were obtained in this study by repeatedly positioning the probe and measuring traces like the one shown in Fig. 8. This was accomplished using a digital electrometer, transferring the associated data to a computer, plotting them and then analyzing them graphically to determine the potential at the probe location. The same procedure was used to obtain profiles along a beamlet centerline and a parallel path that passed through an accel-grid web center. In the latter case, some of the filament emission current v. potential traces would exhibit negative currents (i.e. electron collection) at filament potentials above local potential because there were electrons but no beamlet ions there.

Some measurements were made by simply sensing the potential at which the probe floated as it was swept through the beamlets at various axial locations. The "probe floating potential" sensed by such a probe is generally not the local potential. As Fig. 8 suggests, this potential (i.e. the one where the straight-line electron collection portion of the trace would cross the horizontal axis) can be substantially greater than the local potential when the probe is in an ion beamlet and insufficient electrons are present. Far downstream of the accel grid, however, where the beamlets are neutralized and the electron density is substantial, the probe was observed to float close to the local plasma potential determined from inflection point analysis as expected. Thus, the axial location

at which probe floating potential comes into agreement with local potential is probably close to the location at which beamlets have been neutralized.

## **Results**

### Comparative Erosion Data for Molybdenum and Graphite Accel Grids

Sputter erosion patterns observed on the downstream surface of a 19-hole molybdenum accel grid after 50 hr. of operation at the conditions indicated in the upper portion of Table 1 are shown in Fig. 9. The grid surface appeared uniform before operation so this figure clearly shows that the impingement of low-energy ions produces erosion rings around each aperture in the grid set that are similar to those predicted by Peng, et.al [4]. The radii of these rings appear to increase toward the outside of the outermost holes. There is evidence that pits develop where the rings overlap at the web centers surrounding the center aperture (upper half of grid) and more diffuse erosion patterns can be seen extending radially outward from webs between the outermost holes (lower half of grid). Both the pits and radial erosion patterns are present on the upper and lower halves of the grid, but lighting constraints make it difficult to see them both on a single photograph. The patterns shown in Fig. 9 are also similar to patterns observed after several-hundred-hour life tests conducted on 30 cm dia. divergent and ring-cusp ion thrusters [12,13]. In contrast to the molybdenum accel grid, it was

Table 1  
50 Hour Erosion Test Operating Conditions and Results

Symbol	Variable Description	Value
$V_+$	Screen Grid Potential	1000 V
$V_-$	Accel Grid Potential	-800 V
$\dot{m}_T$	Total Thruster Flow Rate	39 mA eq.
$\dot{m}_N$	Neutralizer Flow Rate	46 mA eq.
$J_D$	Discharge Current	4.5 A
$V_D$	Discharge Voltage	32.5 V
$J_K$	Keeper Current	300 mA
$V_K$	Keeper Voltage	10 V
$J_B$	Beam Current	4.3 mA
$\eta_u$	Propellant Utilization	11 %
$J_{i,d}$	Measured Impingement Current	100 $\mu$ A
$V_B$	Neutralizer Bias Voltage	-15 V
$J_N$	Neutralizer Discharge Current	300 mA
$V_N$	Neutralizer Discharge Voltage	20 V
$P_o$	Ambient Tank Pressure	$7 \times 10^{-6}$ Torr
$\Delta m_{Mo}$	Molybdenum Accel Grid Mass Loss	20.67 mg
$\Delta m_C$	Graphite Accel Grid Mass Loss	2.47 mg
$R_{Mo}$	Mean Molybdenum Erosion Rate	0.61 $\mu$ m/hr
$R_C$	Mean Graphite Erosion Rate	0.41 $\mu$ m/hr
$\gamma_{Mo}$	Molybdenum Sputter Yield*	1.2/1.4
$\gamma_C$	Graphite Sputter Yield*	1.1/0.35

\* Computed Value/Published Value in [14]

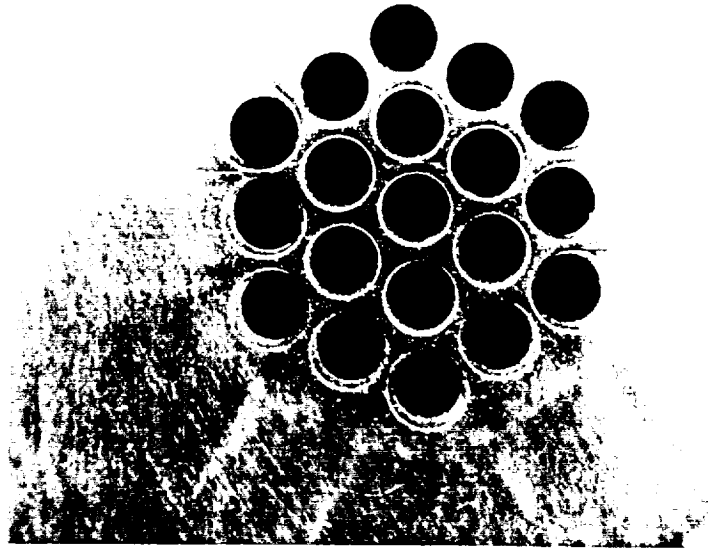


Fig. 9      Photograph of Molybdenum Grid - 50 hr Erosion Test

difficult to see any change in the appearance of the graphite accel grid after 50 hr. of operation.

A typical comparison of depth profiles measured at the edge of the hole pattern for the two accel grids is shown in Fig. 10. As the sketch at the top of the figure indicates, the profiles were measured along paths from the more pristine regions of the grids inward past a pair of apertures in the outermost row to the edge of a hole in the next row. The data show that in this region most of the erosion occurs in the webbing between adjacent holes and that molybdenum erodes more rapidly than graphite. It is believed that the difference in slopes at the edges of the holes is influenced more by the hole-drilling process and the profilometer stylus orientation than by sputter erosion. A similar comparison of typical depth profiles made along paths that terminate at the central holes for the two grid materials is shown in Fig. 11. Absolute depths cannot be compared from these profiles because the entire region profiled may have been eroded and there is, therefore, no common reference height. The profiles do, however, show evidence of the pit seen near the web center in Fig. 9 and the magnitudes of the variations also suggest molybdenum sputter erodes more rapidly than graphite.

The mass losses determined for the two accel grids by weighing them before and after the 50 hr. periods of operation are given in the bottom portion of Table 1. The mean erosion rate given in the table was computed assuming uniform erosion over the downstream accel grid surface within a circle that circumscribes the outer holes (12.7 mm dia). These rates, which are meaningful only in a relative sense because the erosion is clearly not uniform, indicate that substantially different mass losses translate

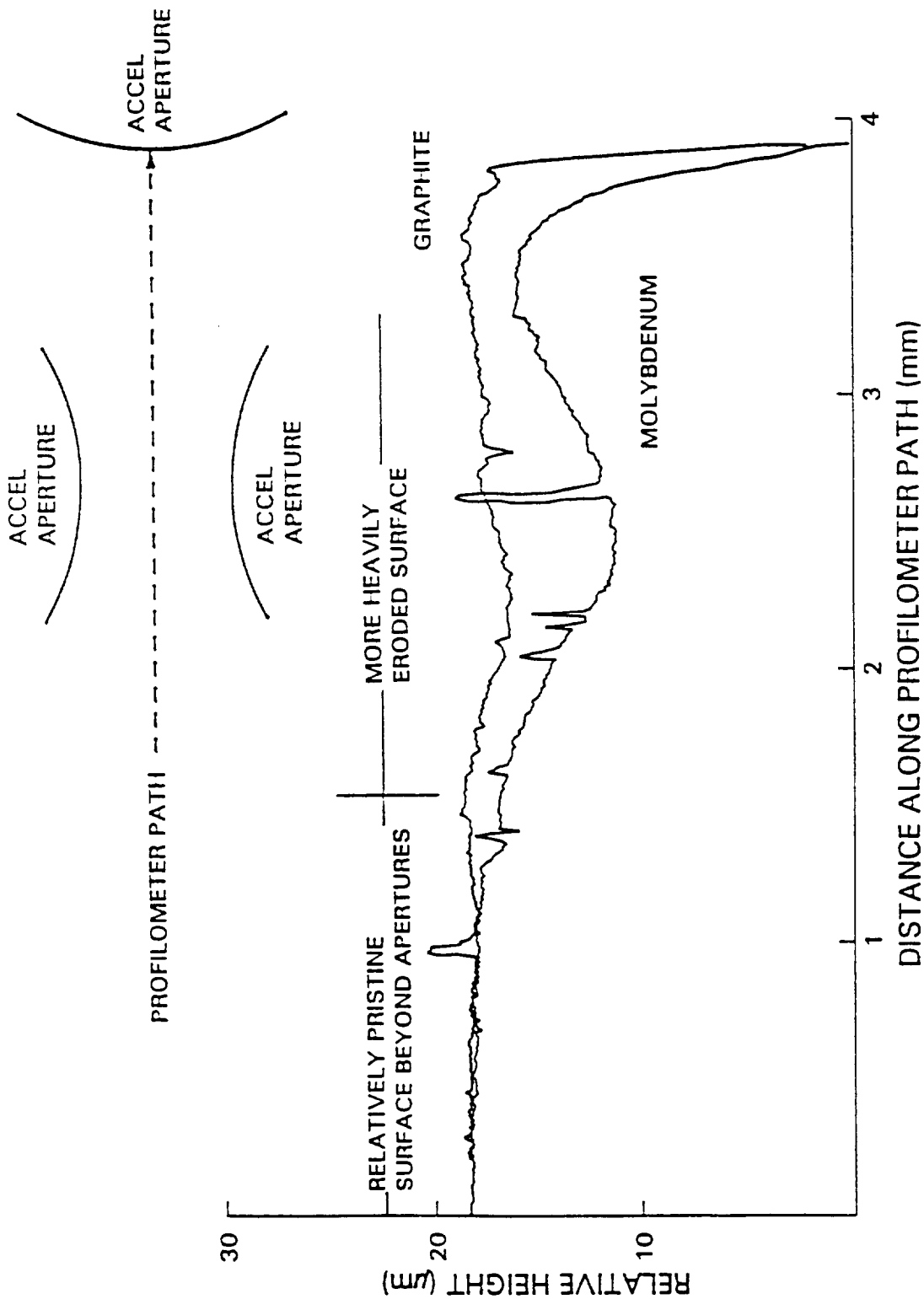


Fig. 10 Erosion Depth Profiles at Outer Apertures - 50 hr Test

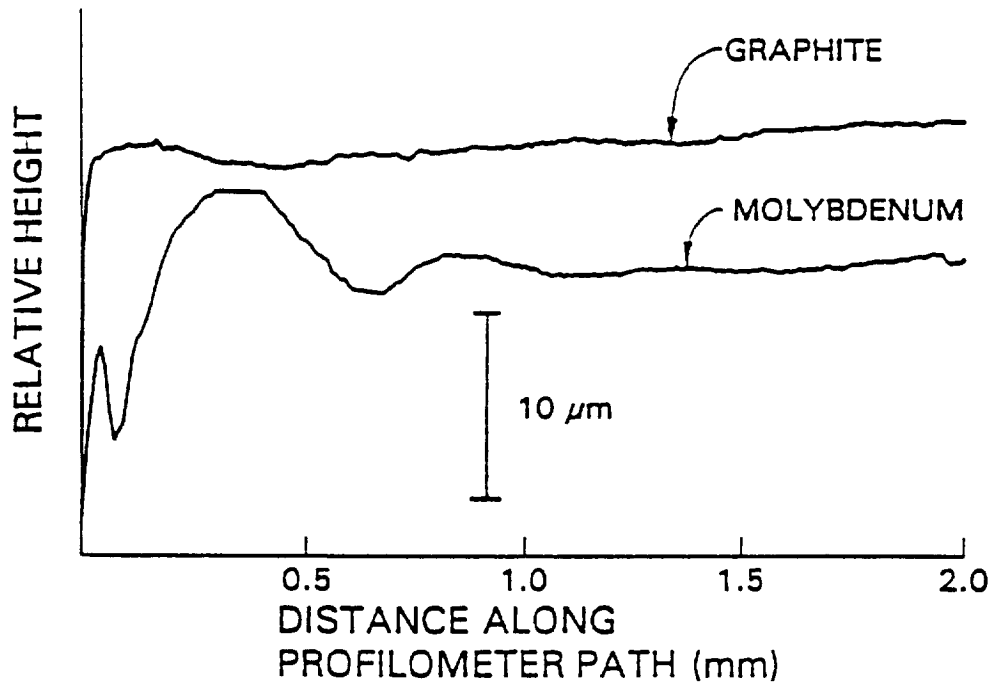
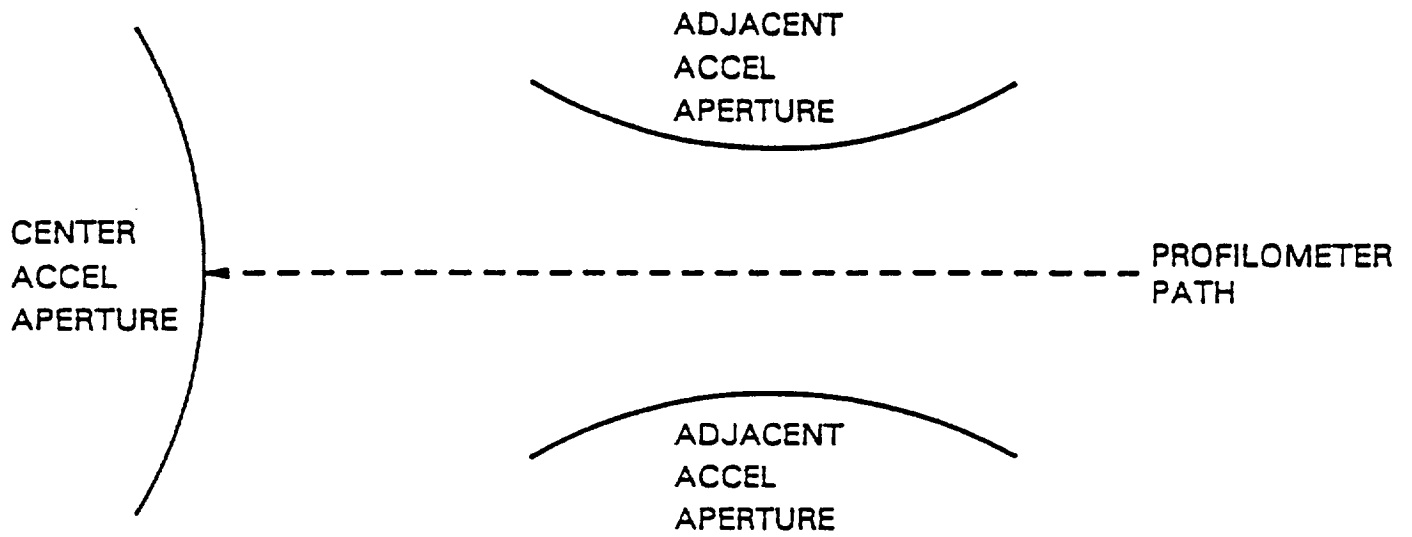


Fig. 11 Erosion Depth Profiles near Central Aperture - 50 hr Test (Absolute Height Comparisons between Profiles are not Meaningful)

into similar erosion rates because the density of molybdenum is 5.7 times that of the graphite. Sputter yields were also computed from the mass losses by computing total atom losses and dividing them by the integrated impingement current over the 50 hr. tests (assuming singly-charged impingement ions). These yields are compared to published data [14] on the last rows of Table 1. The computed molybdenum yield agrees reasonably well with the published value, but the computed value for graphite is three times the published one. A similar discrepancy exists between mean erosion rates computed from the mass losses for graphite and molybdenum (they are about the same, while the profilometric data of Figs. 10 and 11 both suggest molybdenum erodes more rapidly). These discrepancies could be resolved by a graphite accel grid mass loss about one third of the value given in Table 1. Such a discrepancy is possible because the graphite-grid mass loss was small and a significant fraction could have been lost by a mechanism other than sputtering. For example, significant intra-grid arcing was observed during the graphite grid test and mass loss resulting from this or possibly a small scratch made during grid handling could easily account for such a mass loss.

It is also noteworthy that the mean erosion depths determined from the mass losses for the 50 hr. tests would be  $\sim 30$  and  $20 \mu\text{m}$  for molybdenum and graphite, respectively ( $\sim 30$  and  $7 \mu\text{m}$  if the graphite mass loss is reduced to conform to the expected sputter yield as discussed in the preceding paragraph). Since measured height profiles indicate height variations less than  $10 \mu\text{m}$  near the edge holes (Fig. 10), the mass loss results associated with the molybdenum grids also suggest more substantial erosion of the webbing surface occurred near the inner accel grid hole.

## Effect of Gas Backfill on Impingement Current

In order to demonstrate the relative importance of the charge-exchange and electron-impact impingement-ion-production mechanisms, the effects of xenon and argon backfilled into the vacuum chamber on impingement ion production were compared when the 7-hole grid set was being used. The usefulness of such an experiment can be understood by recognizing two facts. First, the neutral densities in Eq. 5 can be expressed as the sum of two components: one due to xenon propellant atoms and the other due to backfilled xenon or argon atoms. Second, the charge-exchange cross-section ( $\sigma_{ce}$ ) for xenon ions with xenon atoms is more than an order-of-magnitude greater than the one for xenon ions with argon atoms [9] while the electron-impact-ionization cross sections ( $\sigma_e$ ) for the two gases are about the same [15] in the expected electron-energy range. The measured effects of xenon and argon backfill on the impingement current when the propellant flow rate and beam current were held constant are compared in Fig. 12. The fact that xenon backfill induces a dramatic increase in impingement current while argon backfill does not demonstrates that low-energy ion production by electron-impact-ionization is small compared to charge-exchange production. If this were not so, the nearly-equal electron-impact-ionization cross-sections for xenon and argon would yield a more substantial effect for the argon backfill case. Consequently, it is argued that the effects of electron-impact ionization (the second integral in Eq. 5) can be neglected.

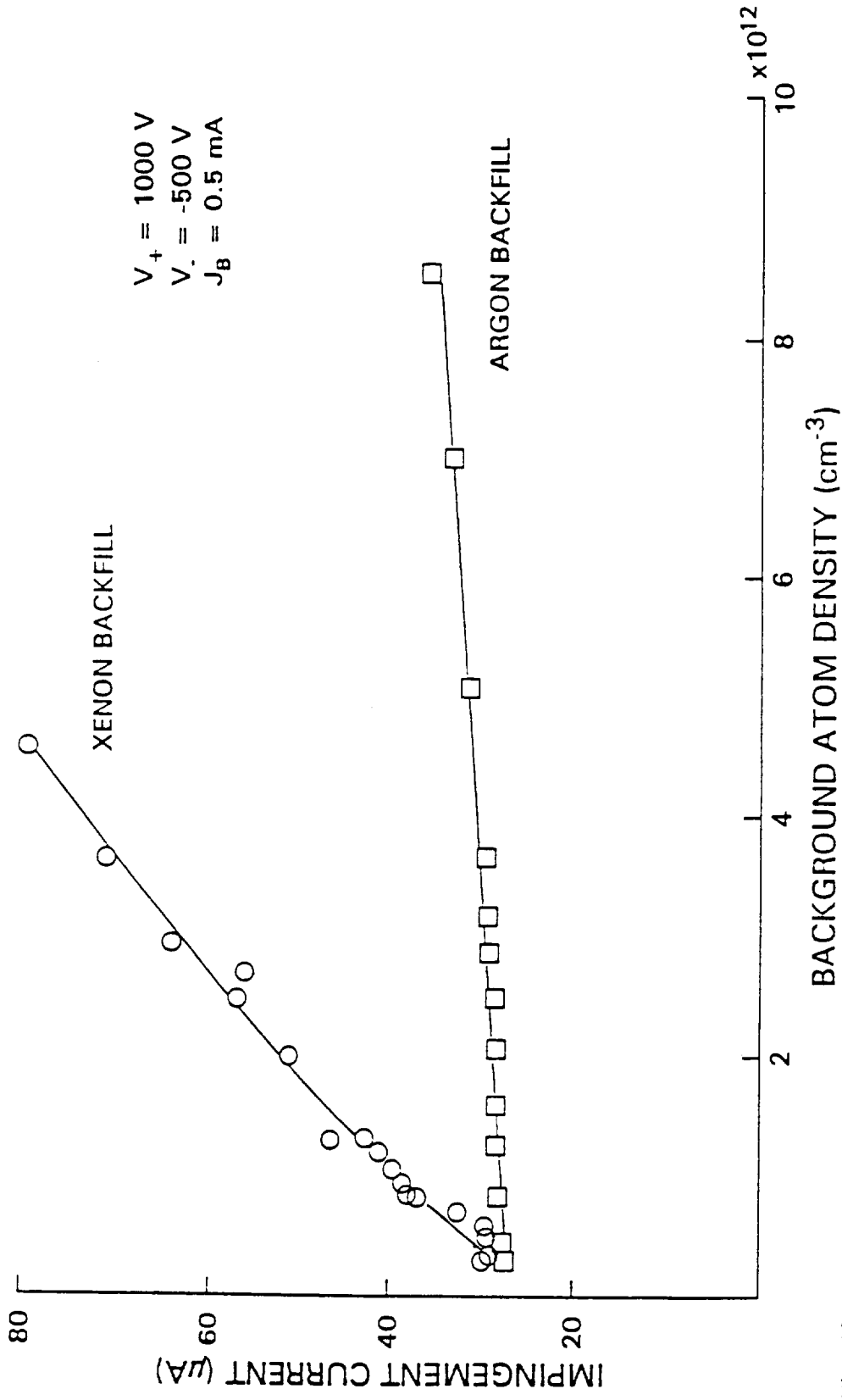


Fig. 12 Effects of Backfill on Impingement Current

## High-Energy Neutral Backflow Experiment

It is possible that high-kinetic-energy neutral atoms backstreaming toward the grids could be ionized downstream of the potential peak (Fig. 1) and that their energy would be sufficient to carry them over this peak, thereby allowing them to reach the accel grid. They would then contribute to the measured impingement current even though they were created downstream of the charge-exchange-ion extraction length. The kinetic energy they would require for this to occur depends on the height of the potential hill. Generally, however, one would expect neutral energies substantially greater than the thermal energy normally acquired at tank-wall surfaces would be needed. High-energy neutrals might be created when propellant ions impinge on vacuum chamber walls, are neutralized by an electron from the wall and then leave the wall with an energy somewhere between their high incident energy and a thermal energy determined by the temperature of the wall. To determine if these energetic neutral atoms were being emitted when ions struck target surfaces, the experimental apparatus shown in Fig. 4 was used. It was expected that energetic-background-atom production would be influenced by rotating either the copper or grafoil targets into the 15 cm dia. xenon ion beam being extracted for the experiment. Either surface might be expected to induce an increase in the impingement current because the geometrical probability of energetic propellant atom reflection back to the ion thruster would increase when the beam ions impacted near (42 cm downstream) rather than far (520 cm downstream) from the grids. Higher backflows of energetic atoms should yield greater charge-exchange collision rates

and greater accel grid impingement currents. Two different target materials with radically different sputter yields and charge-transfer characteristics were used because impingement current changes induced by reflected or sputtered atoms from each of them should have been quite different.

Data obtained with the SERT II ion thruster operating at a screen grid voltage,  $V_+$ , of 1000 V, an accel voltage,  $V_-$ , of -500 V, a nominal beam current,  $J_B$ , of  $\sim 234$  mA, a total flow rate,  $\dot{m}_T$  of 270 mA eq. which induced a background pressure,  $P_o$ , of  $2 \times 10^{-5}$  Torr are shown in Fig. 13. Figure 13a presents the time history of the impingement current when either of the two targets (squares  $\sim$  Grafoil, circles  $\sim$  copper) was rotated into the ion beam. It shows an immediate increase in the impingement current from  $\sim 2.1$  mA to  $\sim 2.3$  mA with the Grafoil target (10% increase) and 2.1 to 2.4 mA with the copper one (15% increase). After the initial jumps, the impingement current remains constant with the copper target in place while it continues to rise gradually to 2.6 mA with the Grafoil one. It is noteworthy that vacuum-tank ambient pressure did not jump from its initial value ( $20 \mu\text{Torr}$ ) immediately after either target was placed in the beam. Subsequently, however, it rose slowly, in direct proportion to the increase in impingement current after the Grafoil target had been inserted. On the other hand, the pressure remained constant with the copper one. This suggests that Grafoil outgassing induced by beam heating was the cause of the gradual rise in impingement current that followed the initial jump when it was placed in the beam. Hence, the initial jumps in impingement current are considered the data of principal importance in Fig. 13a.

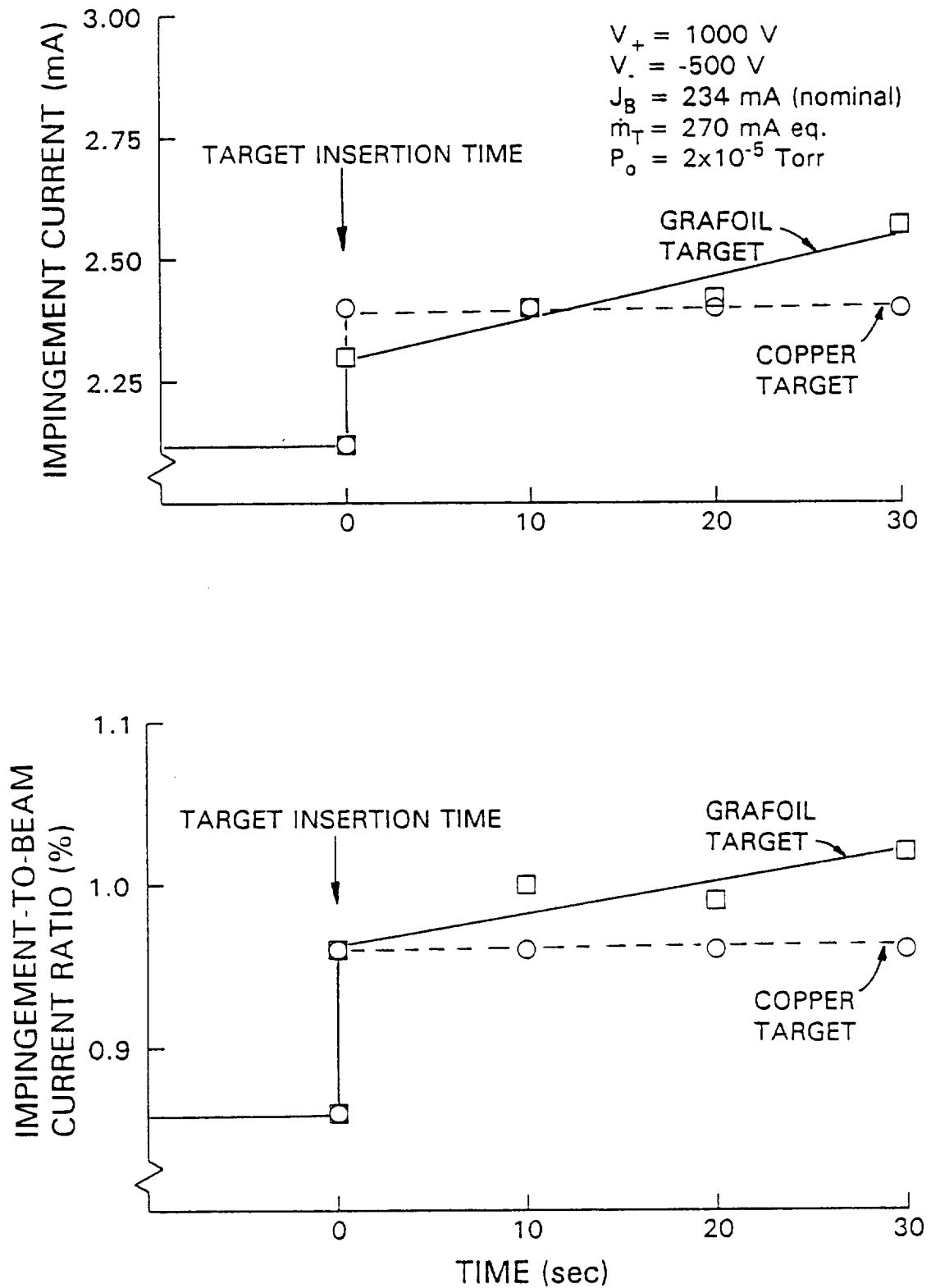


Fig. 13 Effects of Target Insertion on Impingement Behavior

The beam currents changed slightly from the nominal value given on Fig. 13 when either target was rotated into the beam. The data of Fig. 13b show that the ratio of concurrently-measured impingement and beam currents increases abruptly from 0.85% to 0.97% when either target was inserted. Floating emissive probe measurements made between the thruster and the targets indicated the beam-plasma potentials did not change significantly when the targets were rotated into the beam. This suggests that insertion of the targets did not induce an increase in the charge-exchange-ion-extraction length and leads to the conclusion that the measured increase in impingement-to-beam-current ratio must have been due to charge-exchange-ion production from either an increase in the ambient density of low-velocity neutrals or high-energy neutrals backflowing from the targets. Any increase in ambient-neutral density must have been due to either sputtered target atoms, de-absorbed propellant or background atoms or low-velocity-xenon-propellant atoms that were reflected from the target. Such atoms would be expected to leave the targets with thermal velocities. The fact that two target materials with very different sputter yields induced the same impingement-to-beam-current ratio, however, suggests that ions produced from the sputtered-atom contribution is small.

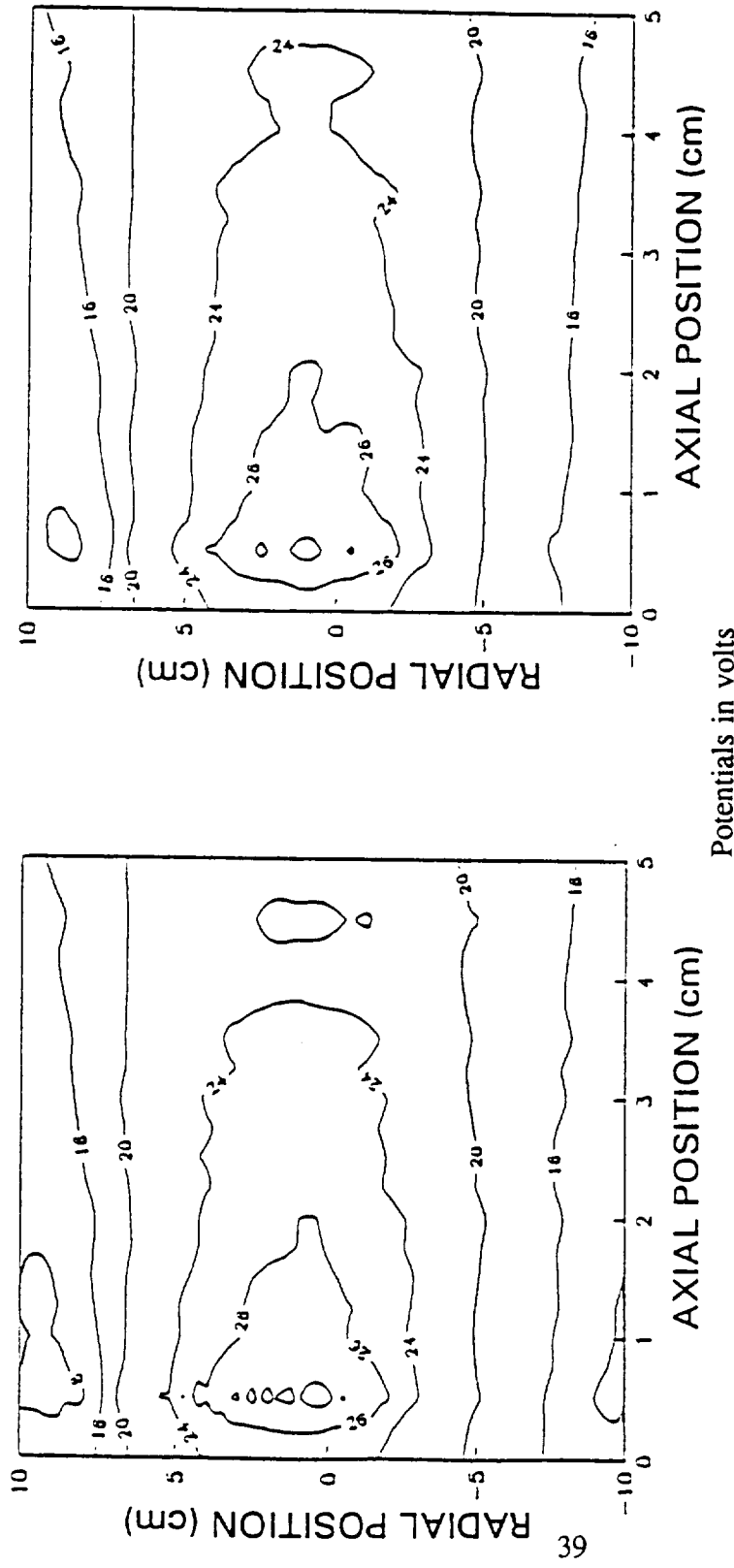
The increase in low-velocity propellant atom density induced by placing either plate in the beam was computed using the numerical code developed to describe flow through the thruster grids. The 10 to 15% increase in neutral density near the accel grid determined from this analysis is essentially the same as the percentage increase in the impingement-to-beam-current ratio. In light of Eq. 5, this result suggests that the measured increase in impingement-to-beam-current ratio is due solely to a local increase

in thermal-velocity neutral atom density and that high-energy neutral backflow from the target is insignificant.

### Potential Fluctuation Experiments

In order to determine if fluctuations in the potentials downstream of the ion thruster could be inducing changes in the charge-exchange-ion-extraction length, the discharge power was changed from the original Sorenson model QRC40-30A power supply to a Sorenson model SRL60-35 power supply. The model SRL60-35 unit was chosen because it has a transistorized, series-regulated output and it operates more stably, i.e., has less ripple when connected to very noisy loads. The power supply change was accomplished quickly, while the thruster flow rates and keeper discharges were maintained. After the change had occurred and the initial high voltage and beam current conditions had been re-established, the directly-measured impingement current ( $J_{id}$ ) was observed to increase slightly from 1.9 to 2.0 mA. Maps of the floating potential field downstream of the accel grid measured immediately before and after the change are compared in Fig. 14. The volume-integrated impingement currents determined by using charge-exchange-ion-extraction lengths obtained from the data of Fig. 14 in Eq. 5 were also unchanged by switching the discharge supply.

In addition, the fluctuations in the current collected by a cold emissive probe being maintained at local plasma potential in the beam were measured before and after the power supply change over the frequency range from 10 Hz to 100 kHz. Analysis of



$J_{1,d} = 1.9 \text{ mA}$   
 $J_{1,v} = 0.14 \text{ mA}$

a) MODEL ORC40-30A

$J_{1,d} = 2.0 \text{ mA}$   
 $J_{1,v} = 0.14 \text{ mA}$

b) MODEL SRL60-35

Fig. 14 Effect of Discharge Power Supply on Floating Potential Maps (15 cm dia. SHAG Optics Beam)

these data using fast Fourier transforms yielded the power spectral density plots shown in Fig. 15. These data suggests that the QRC 40-30A power supply does induce slightly higher plasma noise levels than the SRL 60-35 unit. The results shown in Figs. 14 and 15 suggest, however, that the order-of-magnitude discrepancy between volume-integrated and directly-measured impingement currents is not resolved by using the quieter power supply.

#### Effects of Thruster Operating Conditions on Beamlet Potentials and Impingement Currents

The elimination of secondary electron-emission effects, charge-exchange cross section errors, neutral-propellant-density-profile errors, high-energy backstreaming neutrals and beam plasma noise fluctuations as probable sources of the order-of-magnitude discrepancy between measured and computed impingement currents left charge-exchange ion extraction length as the likely source of the problem. In considering the reasons why this length might be in error it was recognized that the physical dimensions of the probe were larger than the diameter of the accel grid holes in the 15 cm dia. grid set. Hence, its spatial resolution could have been insufficient to yield potentials on the scale needed to determine a charge-exchange-ion-extraction length with sufficient accuracy. It was judged that it would be very difficult to make a smaller emissive probe so detailed potential measurements were made downstream of and through the 7-hole, large-aperture (1 cm dia.) grid set. In order to maximize the beam

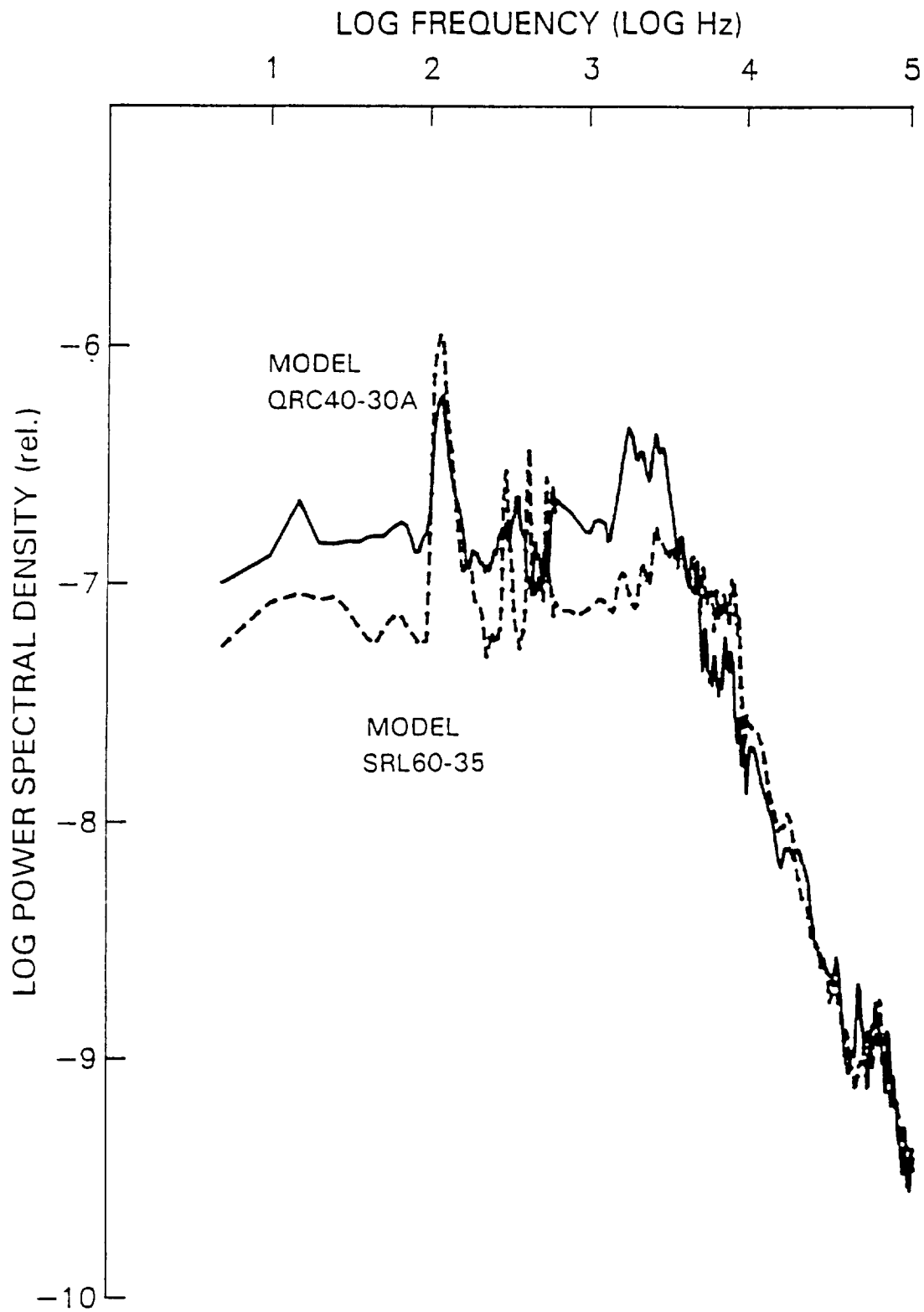


Fig. 15 Power-Spectral-Density Map Comparison

current that could be extracted with grid separation distances that were scaled with the larger hole diameters, the screen and accel grid voltages were increased to what was considered a safe limit with the existing power supplies and high-voltage, vacuum feed-throughs (generally 2000 V and -1000 V, respectively). At these voltages, the 7-hole grid set operated at per-hole beam currents that were similar to those for the original high-perveance set even though beam-ion current densities were much lower. The propellant utilization efficiency at which this thruster operated was also much lower, because a minimum flow rate of  $\sim 45$  mA eq (Xe) was required to sustain hollow cathode and main discharge operation at a reasonable discharge voltage.

Potentials measured using the emissive probe positioned at discrete points along the centerline of the 7-hole grid set at locations ranging from inside the discharge chamber to  $\sim 2$  cm downstream of the accel grid and analyzed using the inflection point analysis are shown in Fig. 16. For this particular test, the experimental data (circles) were obtained at screen and accel grid potentials of 1000 and -500 V, respectively, with no plasma present (zero perveance-per-hole operating condition). The experimental data are compared to a profile computed using a numerical procedure [16] for the same grid potentials. The experimental data behave as expected in that negative potentials on the order of the accel-grid potential are measured near the accel grid and a positive potential equal to the screen-grid potential is measured within the discharge chamber. The computed and measured data also agree well in the intra-grid region, but they depart further downstream because a zero-electric-field boundary-condition is imposed just

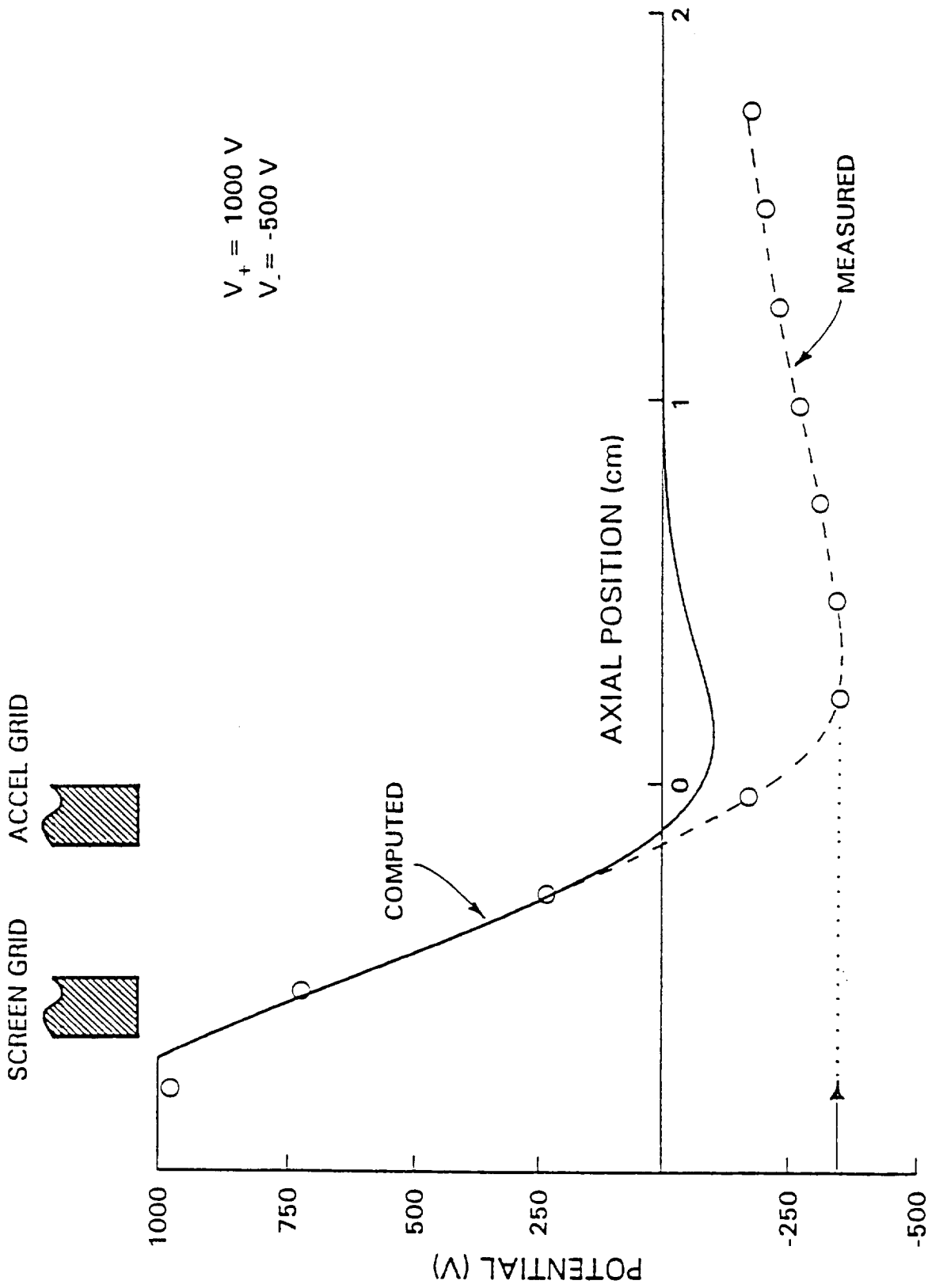


Fig. 16 Computed and Measured Potential Profiles - No Plasma Case

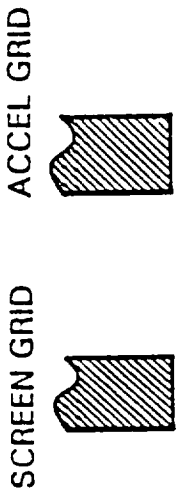
downstream of the accel grid in the numerical solution while this boundary is much further downstream in the experimental case.

In the process of collecting experimental data like that in Fig. 16 it was observed that electrons would be drawn into the discharge chamber from an emissive probe located a few centimeters downstream of the accel grid when the probe was biased negative of the saddle-point potential (the minimum along the aperture centerline--about -350 V in the case of Fig. 16). Subsequently, the same behavior was observed when an ion beam was being extracted and it was recognized that this technique could be used to find the saddle-point potential for an operating thruster. This technique requires that the beam current be monitored at constant thruster operating conditions as the bias on an emissive probe positioned downstream of the grid set is reduced. The bias potential at which the beam current begins to increase (due to electron backstreaming from the probe) is the saddle-point potential.

A second observation made during the collection of the data in Fig. 16 is that an emissive probe positioned upstream of the saddle-point potential will emit electrons readily into the discharge chamber or to the screen grid when it is biased negative of the local potential at the probe location. This emission is again observed as an increase in beam current. For example, a probe located at zero axial position under the electrode potential conditions of Fig. 16 will emit an electron current into the discharge chamber as the probe potential is reduced below about -200 V. One can exploit this behavior to find the axial location for a particular potential between the grids by applying the desired potential to the probe and then moving it upstream until an increase in beam current is

observed. The axial position at which electron emission is first detected on the beam-current meter is the location of the potential of interest.

Potential measurements similar to those of Fig. 16 were next made along the 7-hole accel grid centerline when a 0.5 mA, neutralized beam current was being extracted. A combination of the three techniques described in the preceding paragraphs and in the Apparatus and Procedures section of this report were used to measure the centerline potential profile shown in Fig. 17. This figure presents only that data in the region extending downstream from the first point where intra-grid potentials are substantially positive because it is the potential structure of this region that determines the charge-exchange-ion-extraction length of interest. The open and solid circles designate potentials determined from emissive probe data analyzed using the inflection point technique. No electron backstreaming into the thruster was observed on the beam current meter when the probe was biased  $\sim 50$  V negative of local potential as determined by inflection-point analysis at each of the open-circle points. On the other hand, backstreaming was observed under this bias condition for the solid circle points. The half-solid circle designates the potential at which emission would occur into the discharge chamber from an emissive probe downstream of the saddle-point. Hence, the solid circles designate points upstream of the saddle point while open circles designate points downstream of it and the half-solid circle represents the saddle point itself. The estimated uncertainty associated with the position ( $\pm 0.3$  cm) and potential ( $\pm 10\%$  of the local potential relative to ground) measurements for Fig. 17 are substantial. The data show, however, that potentials rise above ground at negative axial positions, thereby



$V_+ = 1000 \text{ V}$   
 $V_- = -500 \text{ V}$   
 $J_B = 0.5 \text{ mA}$   
 $\dot{m}_T = 46 \text{ mA eq.}$   
 $P_0 = 7 \times 10^{-6} \text{ Torr}$

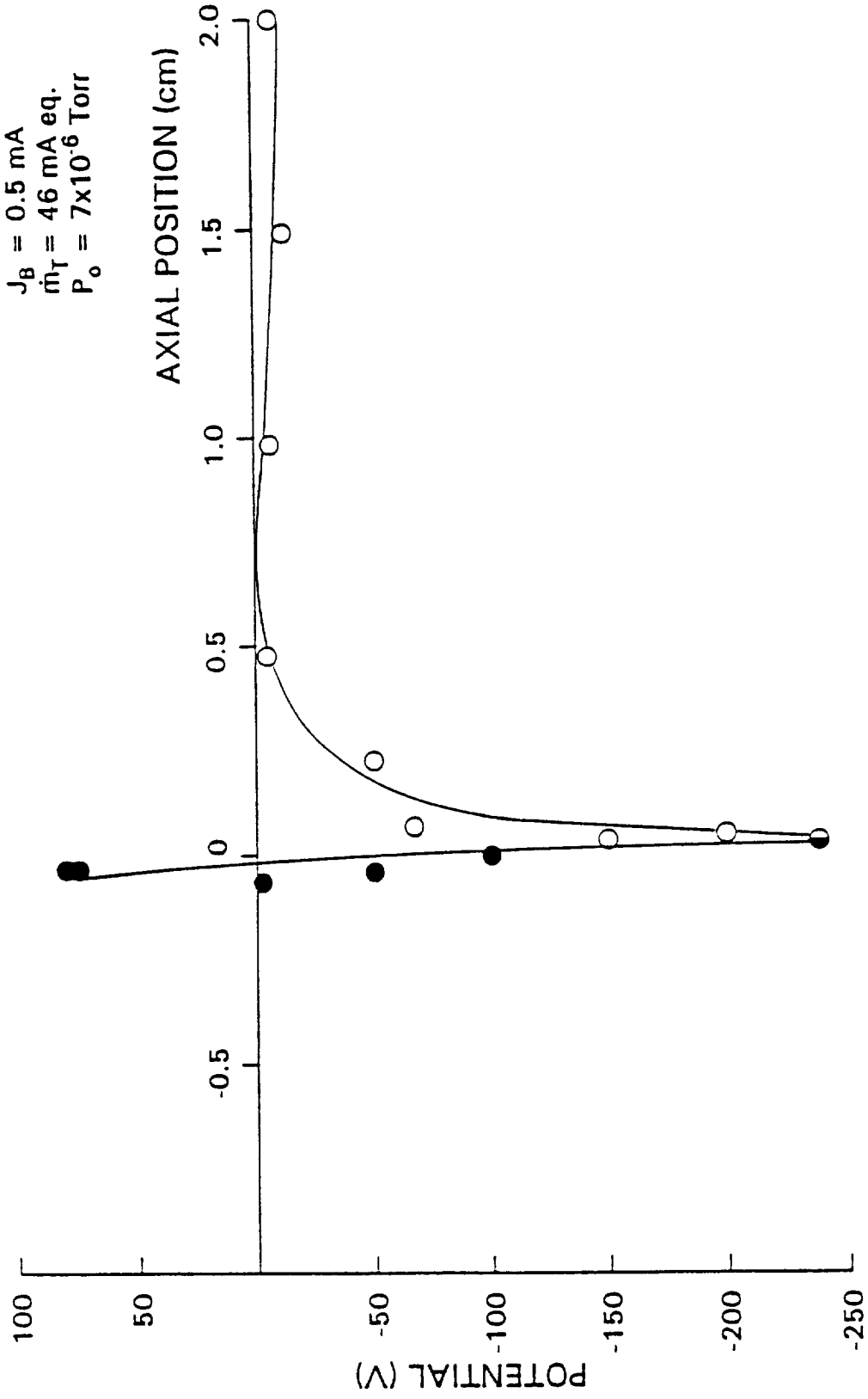


Fig. 17 Centerline Potential Profile with Beam Extraction

suggesting that charge-exchange ions produced upstream of zero will gain sufficient kinetic energy to escape from the accel-grid potential well. This leads, in turn, to the conclusion that the charge-exchange-ion-extraction length ( $\ell_{ce}$ ) can be estimated as the distance from the downstream face of the accel grid (defined to be an axial position of 0) to the downstream potential peak. Because the potential profile is relatively flat downstream of  $\sim 0.5$  cm and the data points are relatively far apart, it is difficult to establish the location of the downstream plasma potential peak from Fig. 17 but it appears to be between 0.5 cm and 1 cm.

Additional potential measurements made over planar surfaces parallel to and downstream of the accel grid revealed that potentials dropped to minimum values at positions over the web centers (Fig. 5). Hence it appeared that the axial potential profiles of greatest interest would be those along the beamlet centerline (beamlet potential profile) and a line parallel to the centerline through a web center (trough potential profile). Typical examples of these profiles measured at the operating condition of Fig. 17 are compared in Fig. 18. These data suggest the beamlet and trough potential profiles coalesce and the downstream plasma-potential peak develops at about the same axial location ( $\sim 1$  cm downstream of the accel grid). Hence, in this typical case, the charge-exchange-ion-extraction length ( $\ell_{ce}$ ) is  $\sim 1$  cm. Using this value together with the value of the charge-exchange cross-section, the beam current and the expected range of neutral density profiles in Eq. 5, a volume-integrated impingement current ( $J_{i\psi}$ ) range between 2.8 and 14  $\mu\text{A}$  is obtained depending on the neutral density assumption. These computed values are substantially less than the measured impingement current (25  $\mu\text{A}$ ).

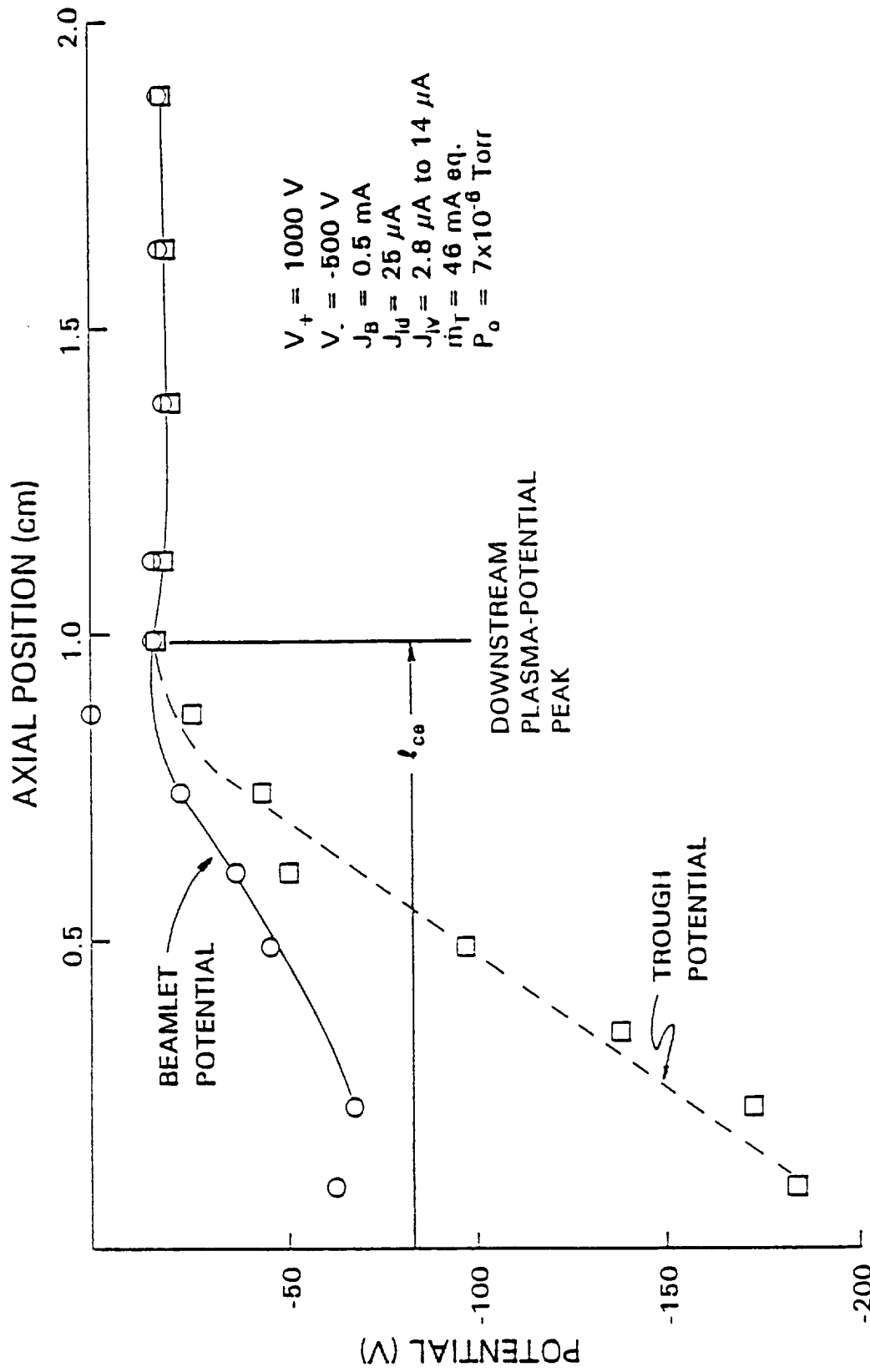


Fig. 18 Typical Beamlet and Trough Potential Profiles

The relative magnitudes of the axial and radial components of the electric fields associated with the trough- and beamlet-centerline-potential profiles in Fig. 17 vary with position. Upstream of the potential peak, however, the axial components for the beamlet and trough are  $\sim 250$  V/cm and about half of this value, respectively. The radial electric fields near the beamlet edges determined from these same data appear to range from zero at the peak to a few hundred V/cm near the accel grid. Under these conditions, charge-exchange ions should travel over axial and radial distances between their points of production and impingement on the accel grid that are of the same order. Such motion is considered consistent with the radial wear patterns that extend beyond the outer holes of the grid as shown in Fig. 9.

Most changes in thruster operating conditions yielded potential profiles that were qualitatively similar to those shown in Fig. 18. When the neutralizer discharge and flow were turned off, however, the potential profiles changed to the extent shown by a comparison of Figs. 18 and 19. Both of the profiles in Fig. 19 rise to positive potentials downstream of the potential peak and the peak is more distinct than that shown in Fig. 18. These higher potentials reflect the effects of ionic space charge and the tendency for the background plasma potential to rise above tank ground in an effort to draw neutralizing electrons from ground-potential surfaces. The reason why the beamlet potential profile would become steeper and essentially match the trough potential profile when the neutralizer is turned off is, on the other hand, not clear. Although turning off the neutralizer induced no change in the measured impingement current ( $25 \mu\text{A}$  for both figures), Fig. 19 suggests it caused  $\ell_{ce}$  to decrease from 1 to 0.8 cm and this in turn

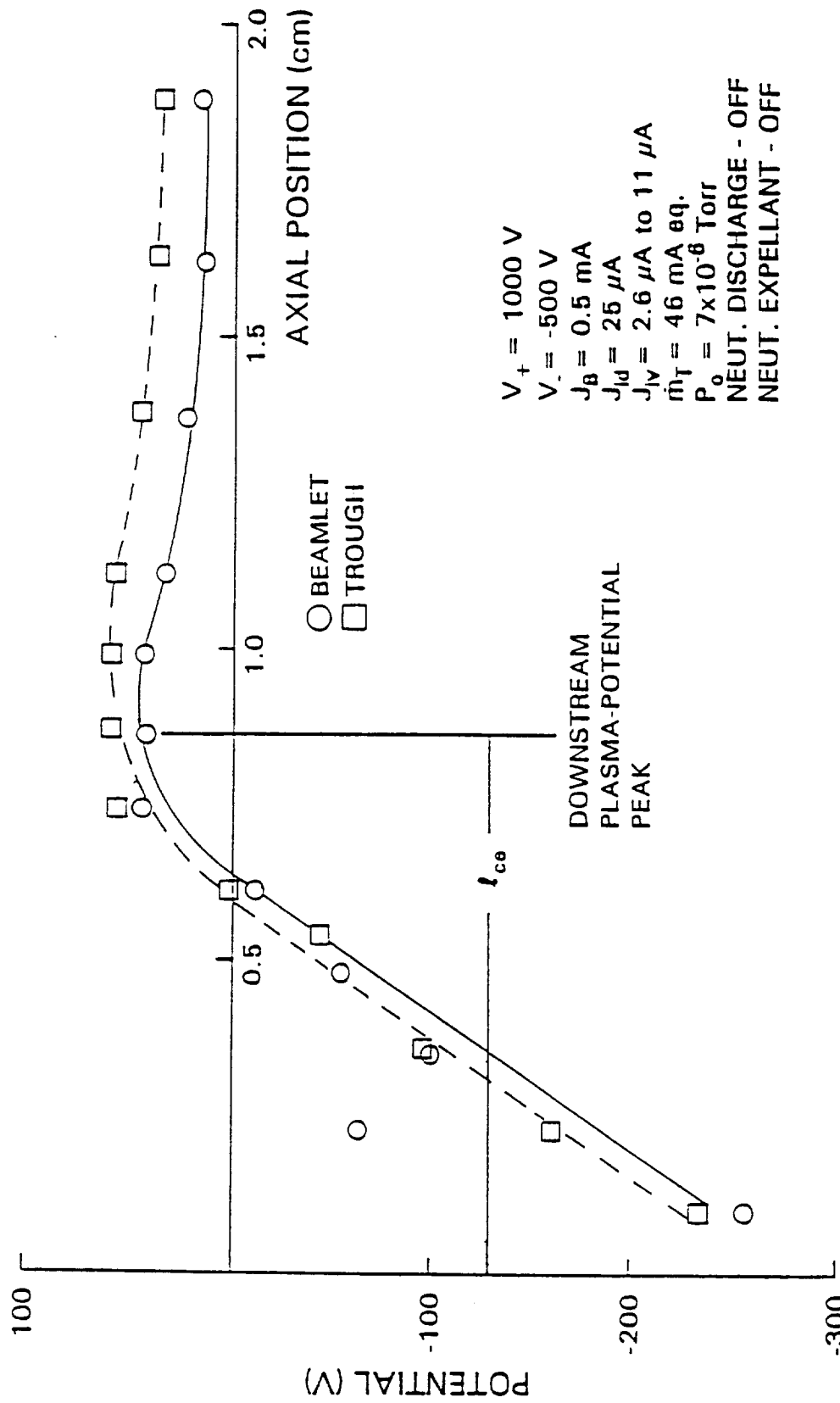


Fig. 19 Beamlet and Trough Potential Profiles - Neutralizer off

causes the maximum volume-integrated impingement current  $J_{iV}$  to drop somewhat from 14 to 11  $\mu\text{A}$ .

Potential profiles like those shown in Fig. 18 were used to determine changes in charge-exchange-ion-extraction length ( $\ell_{ce}$ ) and computed impingement current effected by various changes in thruster and neutralizer operating conditions. For example, Fig. 20 shows that reducing the neutralizer bias voltage from zero to -30 V caused  $\ell_{ce}$  to increase from 0.85 to 1.05 cm. This corresponds to an increase in the maximum computed value of  $J_{iV}$  from 12 to 15  $\mu\text{A}$ , while the measured value remained constant at 35  $\mu\text{A}$ . These results suggest that under these test conditions, the neutralizer bias voltage has a minor effect on impingement current. It is noted that the measured impingement current was observed to change occasionally when the 7-hole grid set was disassembled and reinstalled. This is probably the reason for the difference in impingement currents between Figs. 20 and 18 under essentially identical operating conditions.

The effects of changes in beam current (expressed in terms of a perveance per hole calculated as  $\{J_B/V^{3/2}\}(\ell_e/d_g)^2$  [17] on  $\ell_{ce}$  and the impingement-to-beam current ratio were relatively significant as the data of Fig. 21 show. Except for the charge-exchange-ion-extraction-length data point at  $2 \times 10^{-9} \text{ A/V}^{3/2}$  these data are particularly appealing because they show qualitative agreement between the behaviors of the charge-exchange-ion extraction length and the impingement-to-beam-current ratio. This behavior is predicted by Eq. 5 under the previously demonstrated condition of negligible electron-impact ionization.

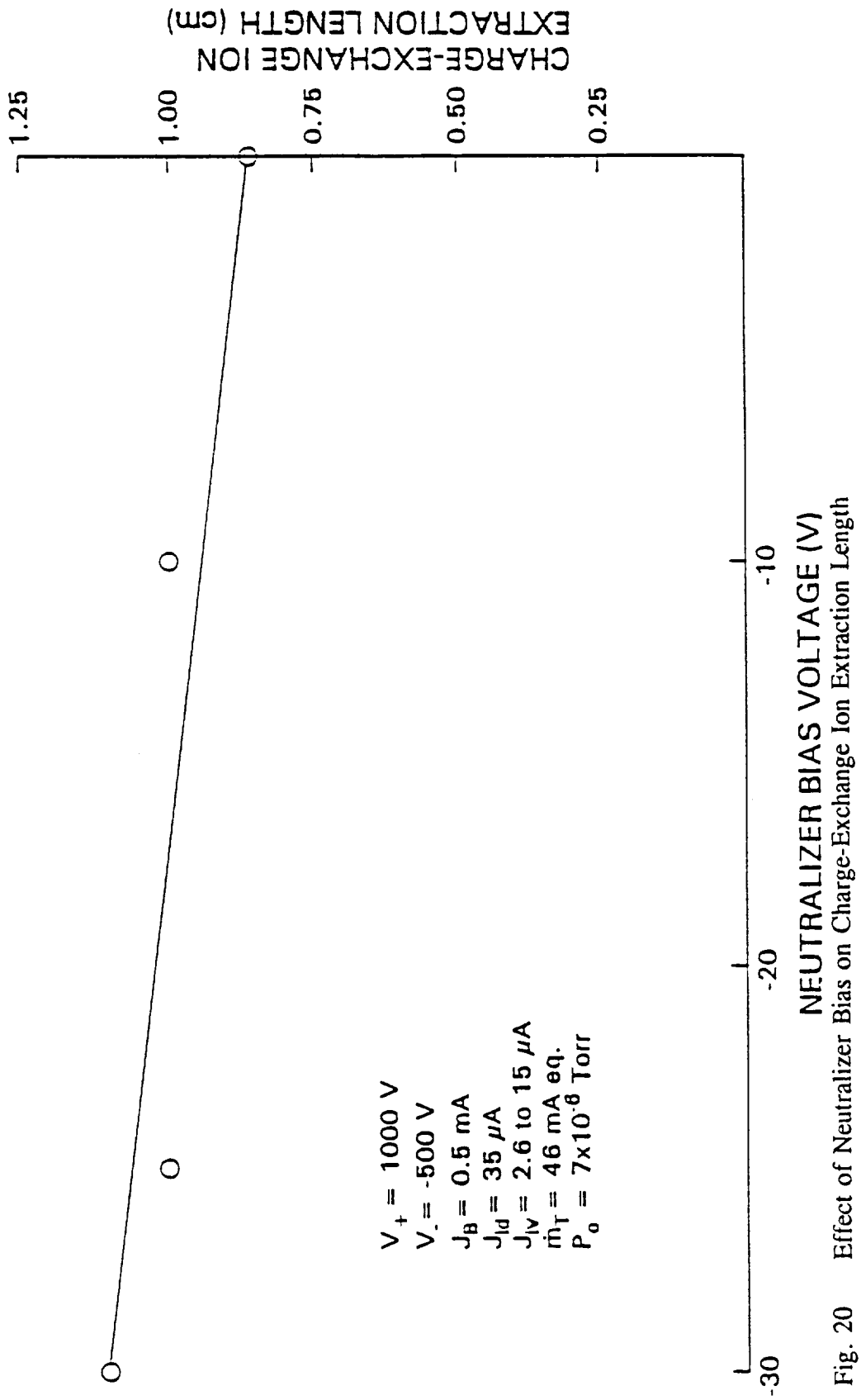


Fig. 20 Effect of Neutralizer Bias on Charge-Exchange Ion Extraction Length

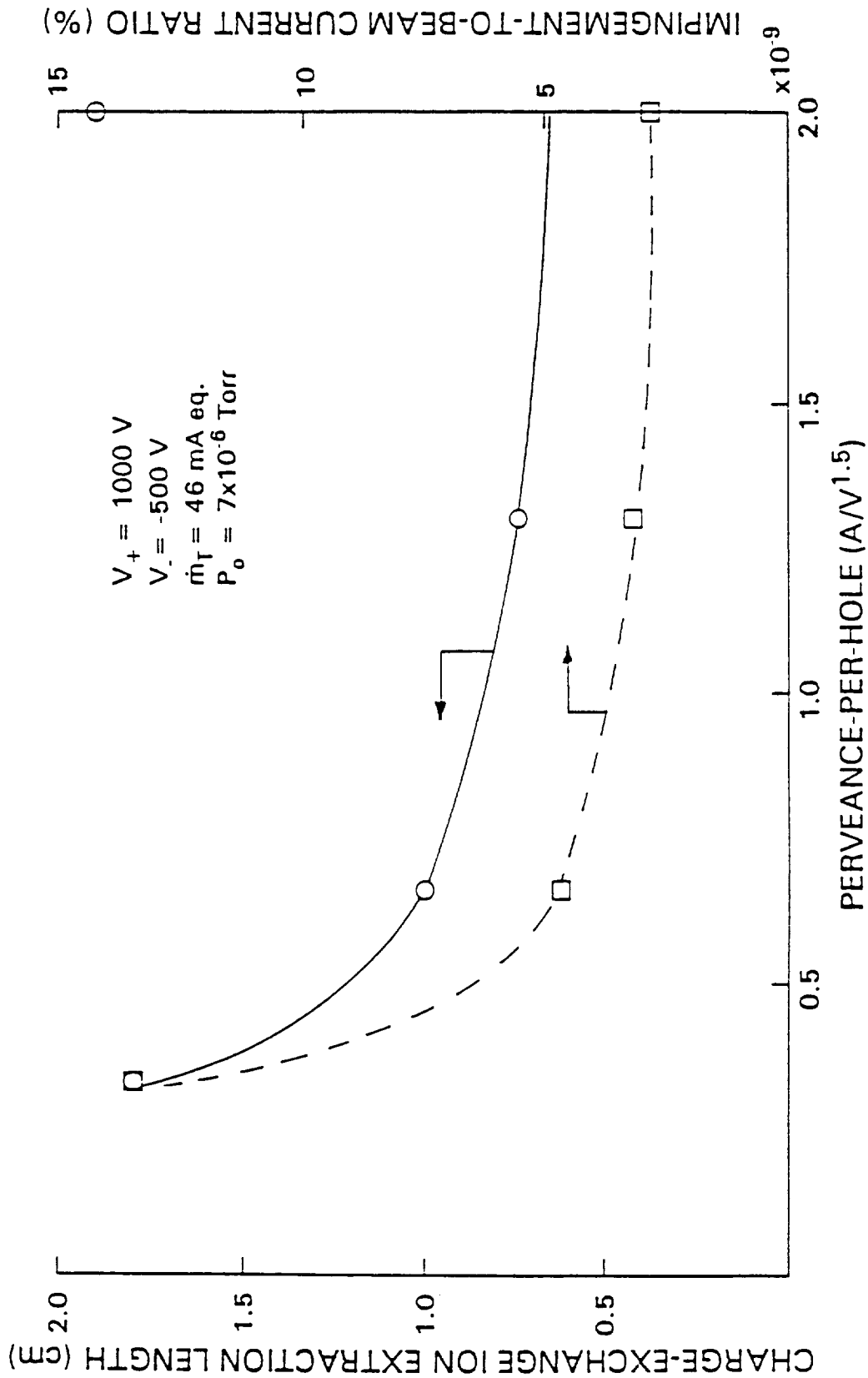


Fig. 21 Effects of Perveance on Charge-Exchange Ion Extraction Length and Impingement-to-Beam Current Ratio

Potential-profile data were also collected at some of the xenon backfill conditions that yielded the data of Fig. 12. Charge-exchange-ion extraction lengths determined from these data are plotted using the left axis of Fig. 22 as a function of background xenon density and a linear dependence is indicated. The impingement currents measured directly and calculated using these lengths are also plotted on the right-hand axis against background xenon density in the same figure. A comparison shows similar qualitative behavior between computed and measured impingement currents, but magnitudes differ substantially. This tendency for measured impingement current to be several times the computed values even when the largest conceivable neutral densities were used was generally observed for all of the data collected in this study.

#### Comparative Floating Potential and Current Density Measurements

Prior to the time the inflection-point method was used to analyze emissive probe data, extensive "floating potential" measurements were made using the a floating emissive probe. Measurements were made at various thruster operating conditions in a region that extended from near the 7-hole accel grid plane to a plane 1.5 cm downstream of it and the Faraday probe was used to collect corresponding current density data. Typical results are given along with the associated thruster operating conditions on Fig. 23 in the form of raised potential and current density plots measured on planes perpendicular to the thruster axis at three downstream axial locations. These data clearly

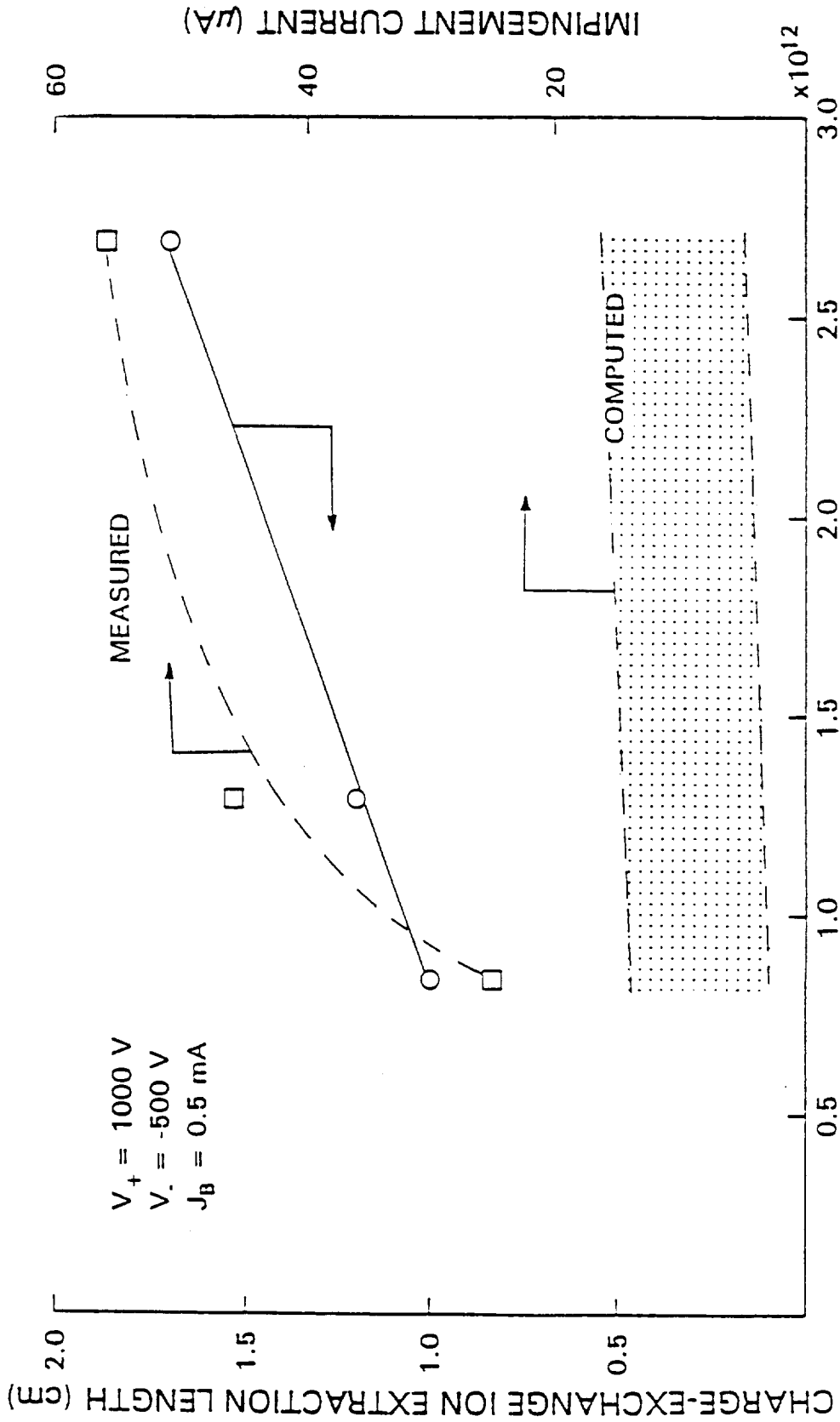
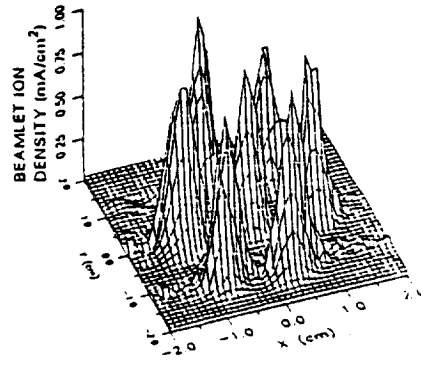
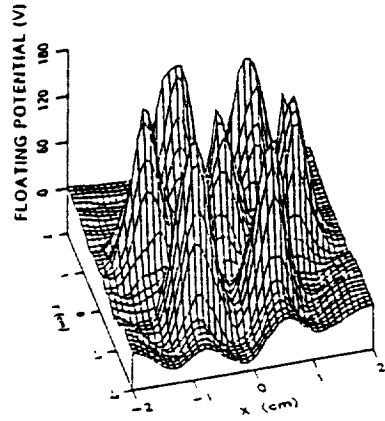
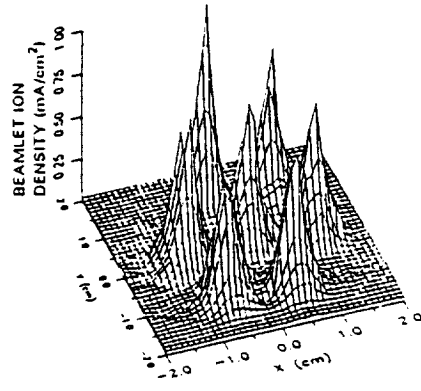
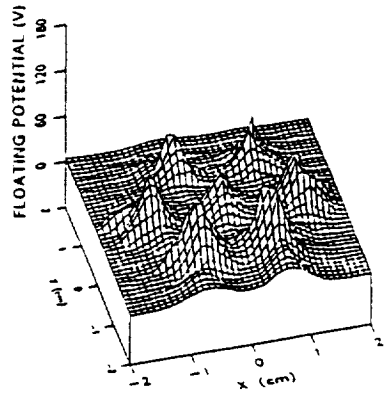


Fig. 22 Effect of Background Xenon Density on Charge-Exchange Length and Impingement Current

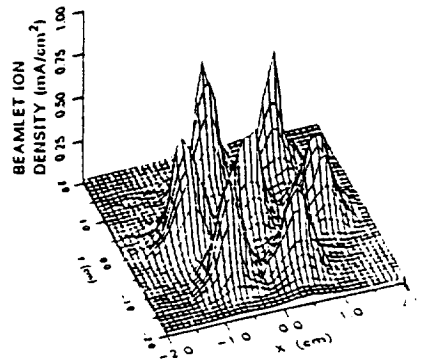
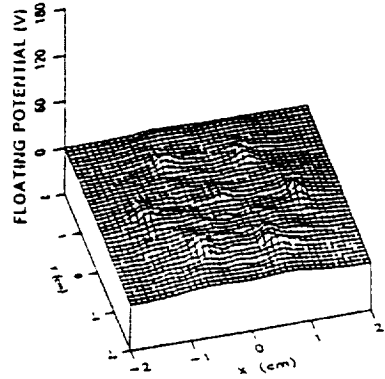
$V_+ = 2000 \text{ V}$   
 $V_- = -1000 \text{ V}$   
 $J_B^- = 1.5 \text{ mA}$   
 $J_{i,d} = 75 \mu\text{A}$   
 $\dot{m}_T = 92 \text{ mA eq.}$   
 $P_0 = 7 \times 10^{-6} \text{ Torr}$



a)  $Z = 0.5 \text{ cm}$



b)  $Z = 1.0 \text{ cm}$



c)  $Z = 1.5 \text{ cm}$

Fig. 23 Comparison of Floating-Potential and Beamlet-Current-Density Maps as a Function of Axial Position

show the seven individual ion beamlets, especially in the right-hand column of plots where the peak magnitudes of the beamlet current densities remain relatively constant at the different downstream axial locations. On the other hand, the beamlet floating potential plots show potential peaks that are high close to the accel grid and decay with downstream axial position. At  $Z = 1.5$  cm, these peaks are barely distinguishable. Taken together, these results indicate that high-energy beamlet ions remain in relatively well-columnated beamlets to a location 1.5 cm downstream of the accel grid. The beamlets become more difficult to distinguish in the downstream floating-potential plots, however, because sufficient neutralizing electrons are present there and they can reach the floating probe and inhibit charging due to high-energy-ion collection on the emissive probe filament. Hence, a floating probe can indicate the locations at which beamlets are being neutralized even though it may not indicate true potentials.

If one assumes that the charge-exchange ion-extraction length is approximately equal to the distance between the accel grid and the location where neutralization has occurred, then the measurements of Fig. 23 provide additional support for a charge-exchange ion-extraction length that is an order of magnitude less than the value required to predict measured impingement currents (i.e.  $\ell_{ce} \sim 1$  cm). These floating-potential measurements therefore support the charge-exchange-ion-extraction-length results obtained from the more accurate plasma potential measurements of Figs. 18 through 22.

## Conclusions

Ions can be produced with low kinetic energies in the vicinity of an accel grid either as a result of electron-impact or charge-exchange processes. These ions contribute to the impingement current on the grid and induce sputter erosion in a pattern of overlapping rings around each accel grid hole. Erosion depth profiles measured using a sensitive profilometer on molybdenum and graphite accel grids tested for 50 hrs. show the molybdenum grid erodes at a rate several times that for the graphite one. Mass loss measurements made on the grids, which suggest similar erosion rates for the two materials, are probably less reliable because the graphite grid ion-erosion-induced mass losses can be similar to those induced by intra-grid arcing and handling.

Under the typical operating conditions investigated in this study, the ions that impinge on the accel grid are produced almost exclusively by charge-exchange collisions between the beamlet ions and neutral propellant atoms that come both from the thruster and the facility. Using grids with large diameter holes, potential profiles that extend along beamlet centerlines and parallel lines passing through web centers can be measured using a small emissive probe. A charge-exchange-ion-extraction length within which charge-exchange ions are drawn into the accel grid can be determined from these measurements. The upstream boundary of the extraction region appears to be located near the downstream plane of the accel grid and the downstream boundary is at the peak in the beamlet-centerline-potential profile. Data suggest that the extraction length is relatively insensitive to neutralizer operating conditions, but it tends to increase with

reductions in beam current and increases in ambient-neutral-atom background pressure. A simple 1-D model of charge-exchange-ion production predicts the generally observed qualitative behavior of impingement current with beam current and background pressure. Before the model can be used to explain differences in the impingement currents associated with thrusters operating on inert gas and mercury propellants, better quantitative agreement with experimental results must be demonstrated. Such efforts should probably focus on improving the accuracy of charge-exchange-ion-extraction-length measurements and ensuring that electron-impact-ionization effects are indeed negligible as preliminary results have suggested.

## References

1. Patterson, M.J., "Low- $I_{sp}$  Derated Ion Thruster Operation," AIAA Paper 92-3203, July 6-8 1992, Nashville, TN.
2. Kerslake, W.R., "Charge-Exchange Effects on the Accelerator Impingement of an Electron-Bombardment Ion Rocket," NASA TN D-1657, May 1963.
3. Monheiser, J.M., "Advanced Electric Propulsion Research - 1990," NASA CR-187103, May 1991.
4. Peng, X., Ruyten, W.M., Keefer, D., "Three-Dimensional Particle Simulation of Grid Erosion in Ion Thrusters," AIAA Paper IEPC-91-119, October 1991, Viareggio, Italy.
5. Child, C.D., "Discharge from Hot Ca0", Phys. Rev., V. 32, May 1911.
6. Knudsen, M., Kinetic Theory of Gases, Methuen & Co. Ltd., London, 1933.
7. Wilbur, P.J., "Advanced Electric Propulsion Research," NASA CR-182130, Jan. 1988, pp. 53-63.
8. Magnuson, G.D. and Carlson, C.E., "Electron Ejection from Metals due to 1- to 10-keV Noble Gas Ion Bombardment. I. Polycrystalline Materials," Physical Review, Vol. 126, No. 6, March 15, 1963, pp. 2403-2408.
9. Rapp, D. and Francis, W.E., "Charge-Exchange between Gaseous Ions and Atoms," The Journal of Chemical Physics, Vol. 37, No. 11, Dec. 1962, pp. 2631-2645.
10. Williams, J.D., "Plasma Contactor Research - 1990," NASA CR-187097, Jan. 1991.
11. Smith, J.R., Hershkowitz, N., Coakley, P., Review of Scientific Instruments, "Inflection-Point Method of Interpreting Emissive Probe Characteristics," Vol. 50, No. 2, Feb. 1979, pp. 210-218.
12. Rawlin, V.K., "Internal Erosion Rates of a 10-kW Xenon Ion Thruster," AIAA Paper-88-2912, July 11-13, 1988, Boston, MA.
13. Patterson, M.J. and T.R. Verhey, "5kW Xenon Ion Thruster Lifetest," AIAA Paper-90-2543, July 18-20, 1990, Orlando, FL.

14. Wehner, G.K., "Sputtering Yield Data in the 100-600 eV Energy Range," General Mills Report 2309, July 15, 1962.
15. Kieffer, L.J., "A Compilation of Electron Collision Cross Section Data for Modeling Gas Discharge Lasers," Joint Institute for Laboratory Astrophysics Report 13, Univ. of Colorado, Sept. 30, 1973.
16. Free, B., Owens, J., and Wilbur, P. J., "Variations of Triple-Grid Geometry and Potentials to Alleviate Accel Grid Erosion," AIAA Paper IEPC-91-047, October 14-17, Viareggio, Italy.
17. Aston, G., Kaufman, H.R. and Wilbur, P.J., "Ion Beam Divergence Characteristics of Two-Grid Accelerator Systems," AIAA Journal, Vol. 16, No. 5, May 1978, pp. 516-524.

## Distribution List

### Copies

National Aeronautics and Space Administration  
Washington, DC 20546

Attn:

RP/Mr. Earl E. VanLaningham, MS B600	1
RP/Mr. Gary Bennett, MS B600	1
RP/Mr. Marcus Watkins, MS600	1

National Aeronautics and Space Administration  
Lewis Research Center  
21000 Brookpark Road  
Cleveland, OH 44135

Attn:

Technology Utilization Office, MS 7-3	1
Report Control Office, MS 60-1	1
Library, MS 60-3	2
Dr. M. Goldstein, Chief Scientist, MS 5-9	1
Mr. Dave Byers, MS SPTD-1	1
Mr. Vincent Rawlin, MS SPTD-1	10
Mr. Bruce Banks, MS 302-1	1
Mr. Michael Patterson, MS SPTD-1	1
Mr. Tim Verhey, MS SPTD-1	1
Mr. Jim Sovey, MS SPTD-1	1

National Aeronautics and Space Administration  
Marshall Space Flight Center  
Huntsville, AL 35812

Attn:

Mr. Ralph Carruth, Mail Code ES 53	1
Mr. Jason Vaughn, Mail Code ES 53	1

NASA Scientific and Technical  
Information Facility  
P.O. Box 8757  
Baltimore, MD 21240

Attn:

Accessioning Dept.	1
--------------------	---

Copies

Dept. of the Navy  
Office of Naval Research  
University of New Mexico  
Bandolier Hall West  
Albuquerque, NM 87131  
Attn: G. Max Irving 1

Case Western Reserve University  
10900 Euclid Avenue  
Cleveland, OH 44106  
Attn: Dr. Eli Reshotko 1

Procurement Executive, Ministry of Defense  
Royal Aircraft Establishment  
Farnborough, Hants GU14 6TD  
ENGLAND  
Attn: Dr. D. G. Fearn 1

United Kingdom Atomic Energy Authority  
Culham Laboratory  
Abingdon, Oxfordshire OX143DB  
ENGLAND  
Attn: Dr. A. R. Martin (Rm F4/135) 1

Intelsat  
3400 International Dr. N.W.  
Washington D.C. 20008-3098  
Attn: Mr. Bernard Free, MS 33 1

Air Force Astronautics Lab  
Edwards AFB, CA 93523-5000  
Attn: OLAC PL/RAS/Mr. J. Chris Andrews 1  
PL/VSA/Dr. Robert Vondra 1

	<u>Copies</u>
Giessen University 1st Institute of Physics Giessen, Germany Attn: Professor H.W. Loeb	1
Jet Propulsion Laboratory 4800 Oak Grove Laboratory Pasadena, CA 91109 Attn: Technical Library Dr. John Barnett, MS 125-224 Dr. John R. Brophy, MS 125-224 Dr. Charles Garner, MS 124-224 Dr. John R. Anderson, MS 125-224	1 1 1 1 1
TRW Inc. TRW Systems One Space Park Redondo Beach, CA 90278 Attn: Mr. Sid Zafran	1
National Aeronautics and Space Administration Ames Research Center Moffett Field, CA 94035 Attn: Technical Library	1
National Aeronautics and Space Administration Langley Research Center Langley Field Station Hampton, VA 23365 Attn: Technical Library	1
Hughes Research Laboratories 3011 Malibu Canyon Road Malibu, CA 90265 Attn: Dr. Jay Hyman, MS RL 57 Dr. J. R. Beattie, MS RL 57 Dr. J. N. Matossian, MS RL 57 Dr. J. D. Williams, MS RL 57	1 1 1 1

Copies

Engineering Quadrangle  
Princeton University  
Princeton, NJ 08540

Attn:

Prof. R.G. Jahn

1

Dr. Arnold Kelly

1

Boeing Aerospace Co.  
P. O. Box 3999  
Seattle, WA 98124-2499

Attn:

Dr. J.S. Meserole, MS 82/83

1

Rocket Research Co.  
P. O. Box 97009  
Redmond, WA 98073-9709

Attn:

Mr. William W. Smith

1

Mr. Paul Lichon

1

Dr. Dave King

1

Electrotechnical Laboratory  
1-1-4, Umezono, Tsukuba-Shi  
Ibaraki, 305 JAPAN

Attn:

Dr. Isao Kudo

1

Sandia Laboratories  
P. O. Box 5800  
Albuquerque, NM 87185

Attn:

Mr. Ralph R. Peters, Mail Code 4537

1

Mr. Dean Rovang, Mail Code 1251

1

Ion Tech Inc.  
2330 E. Prospect Road  
Fort Collins, CO 80525

Attn:

Dr. Gerald C. Isaacson

1

Dr. Dan Siegfried

1

Mr. Larry Daniels

1

Copies

EG & G P. O. Box 1625 Idaho Falls, ID 83401 Attn: Dr. G. R. Longhurst, TSA-104	1
Michigan State University East Lansing, MI 48824 Attn: Dr. J. Asmussen Dr. M.C. Hawley	1 1
Aerospace Engineering Department Faculty of Engineering Tokia University Kitakanome, Hiratsuka-shi, Kanagawa-ken, JAPAN 259 Attn: Prof. Itsuro Kimura	1
Department of Electronics Tokyo National Technical College No. 1220-2 Kunugida-cha, Hachioji 193 Toyko, JAPAN Attn: Mr. Susumu Masaki	1
Tuskegee Institute School of Engineering Tuskegee Institute, AL 36088 Attn: Dr. Pradosh Ray	1
Mr. Lee Parker 252 Lexington Road Concord, MA 01741	1
Physics Department Naval Postgraduate School Monterey, CA 93943-5000 Attn: Dr. Chris Olson, Mail Code 61-0S	1

Copies

Martin Marietta Aerospace  
P. O. Box 179  
Denver, CO 80201  
Attn: Dr. Kevin Rudolph, MS S8064 1

S-Cubed  
P. O. Box 1620  
LaJolla, CA 92038  
Attn: Dr. Ira Katz 1

Dept. of Aero. & Astro. Eng.  
101 Transportation Bldg.  
104 South Mathews Ave.  
Urbane, IL 61801-2997  
Attn: Dr. Rodney Burton 1

Teletronix Inc.  
P.O. Box 500  
Beaverton, OR 97077  
Attn: Mr. Curtis Haynes, MS 50-324 1

W.J. Schafer Assoc. Inc.  
1901 North Fort Meyer Dr., Suite No. 800  
Arlington, VA 22209  
Attn: Dr. Herbert Cohen 1

Electric Propulsion Laboratory, Inc.  
440 N. Green St.  
Tehachapi, CA 93561  
Attn: Dr. Graeme Aston 1

Department of Aeronautics  
University of Tokyo  
7-3-1 Hongo, Bunko-ku  
Toyko 113, JAPAN  
Attn: Dr. Yoshihiro Arakawa 1

Copies

National Space Development Agency of Japan  
2-4-1 Humamatsu-cho, Minato-ku  
Toyko 105, JAPAN  
Attn:

Mr. Kenichi Kajiwara  
Propulsion Engineering Group  
Launch Vehicle Dept.

1

National Aerospace Laboratory  
7-44-1 Jindiajigashi-machi, Chofu  
Toyko 182, JAPAN  
Attn:

Mr. Yukio Hayakawa

1

Center for Aerospace Research  
University of Tennessee Space Institute  
Tullahoma, TN 37388-8897  
Attn:

Mr. Verlin Friedly  
Dr. Xiaohang Peng  
Dr. Dennis Keefer

1

1

1

Engineering Research and Consulting  
P.O. Box 417  
Tullahoma, TN 37388  
Attn:

Dr. Y.C.L. Susan Wu

1